University of Dundee

Downregulation of Keap1 confers features of a fasted metabolic state

Knatko, Elena V.; Tatham, Michael H.; Zhang, Ying; Castro, Cecilia; Higgins, Maureen; Dayalan Naidu, Sharadha

iScience

Article

Downregulation of Keap1 Confers Features of a Fasted Metabolic State

Elena V. Knatko,
Michael H.
Tatham, Ying
Zhang, ..., Julian L.
Griffin, Ronald T.
Hay, Albena T.
Dinkova-Kostova

a.dinkovakostova@dundee.ac.
uk

HIGHLIGHTS

Keap1 downregulation in mice increases Ces1 and Acox2 and decreases triglyceride levels

Genetic interference with Keap1/Nrf2 alters the murine lipidome

Reduced expression of Keap1 lowers hepatic levels of acetyl-CoA

Deleting constitutively active Nrf2 decreases tubulin acetylation and autophagic flux

Article

Downregulation of Keap1 Confers Features of a Fasted Metabolic State

Elena V. Knatko,[1,7] Michael H. Tatham,[2,7] Ying Zhang,[1] Cecilia Castro,[3] Maureen Higgins,[1] Sharadha Dayalan Naidu,[1] Chiara Leonardi,[1] Laureano de la Vega,[1] Tadashi Honda,[4] Julian L. Griffin,[3,5] Ronald T. Hay,[2] and Albena T. Dinkova-Kostova[1,6,8,*]

SUMMARY

Transcription factor nuclear factor erythroid 2 p45-related factor 2 (Nrf2) and its main negative regulator, Kelch-like ECH-associated protein 1 (Keap1), are at the interface between redox and intermediary metabolism, allowing adaptation and survival under conditions of oxidative, inflammatory, and metabolic stress. Nrf2 is the principal determinant of redox homeostasis, and contributes to mitochondrial function and integrity and cellular bioenergetics. Using proteomics and lipidomics, we show that genetic downregulation of Keap1 in mice, and the consequent Nrf2 activation to pharmacologically relevant levels, leads to upregulation of carboxylesterase 1 (Ces1) and acyl-CoA oxidase 2 (Acox2), decreases triglyceride levels, and alters the lipidome. This is accompanied by downregulation of hepatic ATP-citrate lyase (Acly) and decreased levels of acetyl-CoA, a trigger for autophagy. These findings suggest that downregulation of Keap1 confers features of a fasted metabolic state, which is an important consideration in the drug development of Keap1-targeting pharmacologic Nrf2 activators.

INTRODUCTION

Kelch-like ECH-associated protein 1 (Keap1) is the mammalian sensor for electrophiles and oxidants and the main negative regulator of transcription factor nuclear factor erythroid 2 p45-related factor 2 (Nrf2, gene name *NFE2L2*). Together, Keap1 and Nrf2 form a tightly coupled sensor/transducer system that orchestrates the expression of a large network of genes encoding proteins, which are essential for adaptation and survival under conditions of oxidative, electrophilic, and inflammatory stress (Yamamoto et al., 2018). Genetic disruption of Nrf2 renders cells and animals much more sensitive to damage by electrophiles, oxidants, and inflammatory agents when compared with their wild-type counterparts; conversely, pharmacologic induction of Nrf2-dependent genes very effectively protects against electrophiles, oxidants, and proinflammatory agents in numerous animal models of chronic disease, and has health benefits in humans (Hayes and Dinkova-Kostova, 2014).

Under homeostatic conditions, Keap1 acts as a substrate adapter of a Cullin RING E3-ubiquitin Ligase (CRL), containing Cul3 and Rbx1, which continuously targets Nrf2 for ubiquitination and proteasomal degradation (Cullinan et al., 2004; Kobayashi et al., 2004; Zhang et al., 2004). In response to electrophiles and oxidants (termed inducers), which recognize and chemically modify specific cysteine residues of Keap1 (Dayalan Naidu and Dinkova-Kostova, 2020; Dinkova-Kostova et al., 2002), ubiquitination of Nrf2 is inhibited, leading to its stabilization and nuclear accumulation. Nuclear Nrf2 coordinately activates transcription of nearly 500 genes (Malhotra et al., 2010), the protein products of which are extraordinarily versatile and, by a range of mechanisms—including direct antioxidant activity, obligatory 2-electron reduction reactions, conjugation with endogenous ligands, recognition, repair and removal of damaged proteins—serve as critical cytoprotective defenses to eliminate a wide variety of potentially damaging agents and to restore redox balance.

In addition to genes encoding a large number of enzymes for drug metabolism, glutathione- and thioredoxin-related biosynthesis, and regeneration, in proliferating cells, such as those in the gastrointestinal epithelium, Nrf2 controls expression of malic enzyme 1 (ME1), isocitrate dehydrogenase 1 (IDH1), and the pentose phosphate pathway (PPP) enzymes glucose-6-phosphate dehydrogenase (G6PDH) and

[1]Jacqui Wood Cancer Centre, Division of Cellular Medicine, School of Medicine, University of Dundee, Dundee, Scotland DD1 9SY, UK

[2]Centre for Gene Regulation and Expression, School of Life Sciences, University of Dundee, Dundee, DD1 5EH, Scotland, UK

[3]Department of Biochemistry and the Cambridge Systems Biology Centre, University of Cambridge, 80 Tennis Court Road, Cambridge, CB2 1QW, UK

[4]Department of Chemistry and Institute of Chemical Biology & Drug Discovery, Stony Brook University, Stony Brook, NY 11794-3400, USA

[5]Section of Biomolecular Medicine, Department of Metabolism, Digestion and Reproduction, Imperial College London, South Kensington, London SW7 2AZ, UK

[6]Department of Pharmacology and Molecular Sciences and Department of Medicine, Johns Hopkins University School of Medicine, Baltimore, MD 21205, USA

[7]The authors contributed equally

[8]Lead Contact

*Correspondence: a.dinkovakostova@dundee.ac.uk

https://doi.org/10.1016/j.isci.2020.101638

6-phosphogluconate dehydrogenase (6PGD) (Mitsuishi et al., 2012; Thimmulappa et al., 2002; Wu et al., 2011); together, these four enzymes are principally responsible for NADPH generation. As NADPH is the main provider of reducing equivalents for redox and biosynthetic reactions, this critical function places Nrf2 at the interface between redox and intermediary metabolism. We previously reported that Nrf2 also affects cellular metabolism by improving mitochondrial function and bioenergetics (Holmstrom et al., 2013), in part by promoting fatty acid oxidation (FAO). In fact, FAO was enhanced in mouse embryonic fibroblast (MEF) cells and isolated mitochondria from Keap1-knockdown (Keap1-KD, with constitutive Nrf2 pathway activation due to downregulation of expression of Keap1) mice, whereas it was impaired in their Nrf2-knockout (Nrf2-KO) counterparts (Ludtmann et al., 2014). To gain further insights of the role of Nrf2 in lipid metabolism, in the current study, we used mitochondria-enriched preparations from the murine liver, an organ of high metabolic activity, and organoids from mouse small intestine, where the majority of the end absorption of nutrients takes place. In addition, some of our investigations included the murine colon, because high-fat diet accelerates progression of colorectal cancer in mice (Cai et al., 2015; Fu et al., 2019), and obesity, the prevalence of which is increasing worldwide (Bluher, 2019), is a colorectal cancer risk factor in humans (Kuipers et al., 2015).

Using proteomics and lipidomics, we demonstrate that downregulation of Keap1 in mice, and consequent Nrf2 activation to pharmacologically relevant levels, leads to induction of carboxylesterase 1 (Ces1) and acyl-CoA oxidase 2 (Acox2), enzymes involved in lipid catabolism; decreases triglyceride levels; and confers a distinct fatty acid profile. At the same time, hepatic ATP-citrate lyase (Acly) is suppressed and levels of its enzymatic product, acetyl coenzyme A (acetyl-CoA), are decreased, which is a trigger for autophagy. Together, these findings suggest that downregulation of Keap1 confers features of a fasted metabolic state. Understanding this is important, as dysregulation (either down- or upregulation) of Keap1/Nrf2 function is associated with disease risk in humans, including chronic obstructive pulmonary disease, cardiovascular and neurodegenerative diseases, as well as cancer (Cho et al., 2015; Quinti et al., 2017; Rojo de la Vega et al., 2018; von Otter et al., 2010). Furthermore, the Keap1/Nrf2 system is now considered a drug target, with a number of small molecule pharmacologic activators currently being in various stages of clinical development (Cuadrado et al., 2019).

RESULTS

Genetic Interference with Keap1/Nrf2 Affects the Abundance of Metabolic Proteins

To identify the protein components of metabolic pathways displaying altered expression in response to genetic interference with Keap1/Nrf2, a proteomic analysis was conducted. Mitochondria were enriched by differential centrifugation from (1) liver and (2) early-passage (p1) intestinal organoids prepared from wild-type (WT), Nrf2-KO, and Keap1-KD mice (Knatko et al., 2015; Taguchi et al., 2010). Proteins from mitochondria-enriched preparations, in triplicate, were separated by SDS-PAGE and visualized by Coomassie staining (Figures 1A and 1B). Tryptic peptides were extracted and analyzed by liquid chromatography-tandem mass spectrometry (LC-MS/MS) with two different run parameters using MaxQuant (Cox and Mann, 2008) for label-free Quantitation and Perseus (Tyanova et al., 2016) for bioinformatic analysis. Principal-component analysis (PCA) showed separation by tissue type (Figure 1C, component 1), as well as by genotype (Figure 1C, component 2), with the WT mouse samples spatially positioned between the two mutants (see Data S1, and Table S1 for details). This is a clear indication of the opposing effects of Nrf2 and Keap1 interference. Individual comparisons of Nrf2-KO and Keap1-KD with WT identified groups of proteins significantly up- or down-regulated by the mutations, however, to simplify further analysis, the ratio of Nrf2-KO/Keap1-KD was used, with any protein whose abundance is dependent on Nrf2 having a low Nrf2-KO/Keap1-KD ratio (or negative $\log_2$ ratio). Volcano plots of these comparisons for each MS run for liver (Figures S1A and S1B) and intestinal organoids (Figures S1C and S1D) indicated that the majority of quantified proteins do not change. A small group of proteins showed significant differences between Nrf2-KO and Keap1-KD genotypes (Figure 1D for liver and 1E for organoids), with nine defined as significantly altered (Student's t test, false discovery rate 0.1, S0 0.1) between the two genotypes in all four MS runs. These include enzymes involved in xenobiotic metabolism, namely, glutathione S-transferase μ1 (Gstm1), carbonyl reductase 1 (Cbr1), the endoplasmic reticulum (ER) enzymes epoxide hydrolase 1 (Ephx1), UDP-glucuronosyltransferase (Ugt2b35), liver carboxylesterase 1 (Ces1), carboxylesterase 1f (Ces1f), and hexose-6-phosphate dehydrogenase (H6pd), the initial enzyme of a PPP inside the ER that generates NADPH for ER enzymes. In addition, NADPH-binding short-chain oxidoreductase family member Htatip2 and endocytic-lysosomal compartment-residing protein Creg1 were also less abundant in the Nrf2-KO compared with the Keap1-KD genotype.
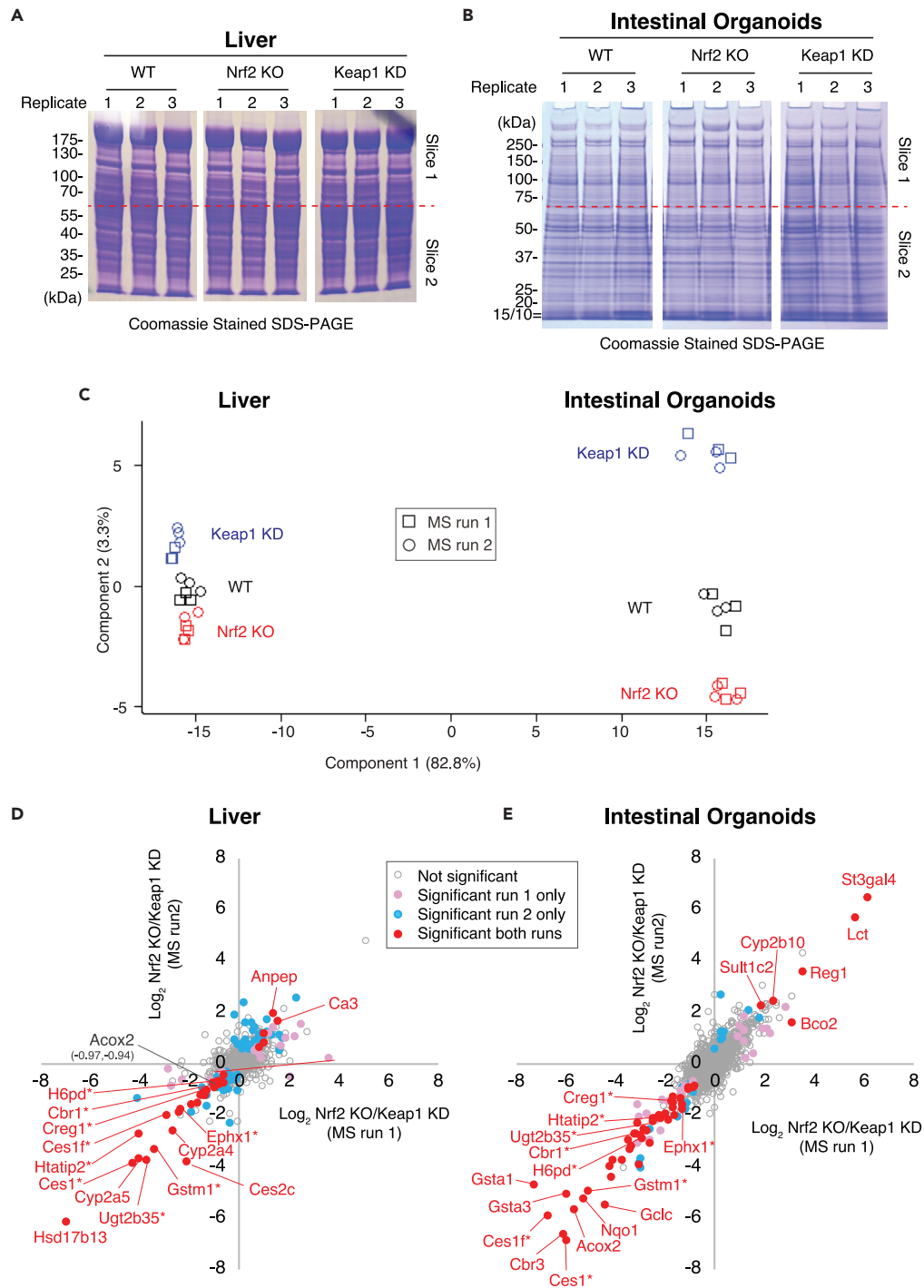
Figure 1. Proteomic Analyses of Mitochondria-Enriched Preparations from Liver and Early-Passage Intestinal Organoids from Wild-Type (WT), Nrf2-Knockout (Nrf2-KO), and Keap1-knockdown (Keap1-KD) Mice

(A and B) Coomassie-stained SDS-PAGE gel of protein samples prepared from mitochondria-enriched fraction from liver (A) or intestinal organoids (B) from mice with the indicated genetic alterations.

(C) Principal-component analysis (PCA) of 906 proteins with intensities reported in all samples in all MS runs in both experimental systems. Normalized LFQ intensities were $\log_2$ transformed and Z-scored by average $\log_2$ LFQ before PCA.

(D and E) Summary of the quantitative data from two MS runs each for the enriched mitochondria samples from liver (D) and intestinal organoids (E). Proteins are colored by statistical criteria for outlier status (see text for statistical methods). Red entries are described further in Tables S1 and S2. The indicated proteins were found in all four MS runs to be
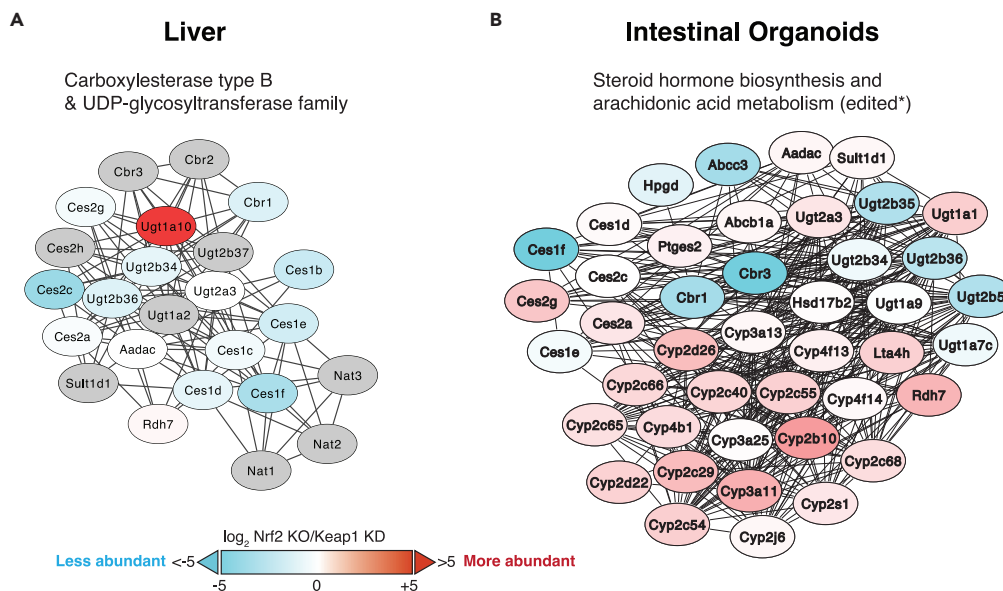
Figure 1. *Continued*

significantly different between Nrf2-KO and Keap1-KD genotypes. Gene names: Cbr1: carbonyl reductase [NADPH] 1, Ces1: liver carboxylesterase 1, Ces1f: carboxylesterase 1F, Creg1: protein CREG1, Ephx1: epoxide hydrolase 1, Gstm1: glutathione S-transferase Mu 1, H6pd: GDH/6PGL endoplasmic bifunctional protein, Htatip2: oxidoreductase HTATIP2, Ugt2b35: UDP-glucuronosyltransferase. All data can be found in Data S1, Quantitative proteomics data. See also Figure S1.

To extract more general biological patterns, STRING analysis was used to determine if any functionally related proteins showed similar changes between the two genotypes. Samples derived from liver provided fewer protein identifications and fewer functional enrichments than those from organoids. Liver network clusters with the highest enrichment score contained a number of carboxylesterases (Ces1 members) and UDP-glucuronosyltransferases (Ugt proteins), with lower abundances in Nrf2-KO (Figure 2A; see also Data S2, STRING functional group enrichment analysis, related to Figures 2 and 3, and Table S2). Curiously, an exception among members of the Ugt family of enzymes was Ugt1a10, the abundance of which was higher in Nrf2-KO than Keap1-KD. As transcription of Ugt1a10 is regulated by both Nrf2 and the aryl hydrocarbon receptor (AhR) (Kalthoff et al., 2010) and the two transcription factors engage in crosstalk (Hayes et al., 2009; Yeager et al., 2009), this finding suggests that binding of AhR to the promoter of Ugt1a10, and consequently its expression, might be enhanced in the absence of Nrf2. Few other networks showed coordinated changes in liver samples, although clusters of proteins with roles in protein processing in ER and signal peptidase complex (Figure S2A) and proteins involved in mitochondrial complex I biogenesis (Figure S2B) showed quantitatively modest, but statistically significant differences.

In organoids, due to the greater differences between the genotypes, it was possible to identify a higher number of significant network clusters. In close agreement with the liver data, organoid network clusters with the highest enrichment score also contained carboxylesterases (Ces1 members) and UDP-glucuronosyltransferases (Ugt proteins), with lower abundances in Nrf2-KO compared with Keap1-KD (Figure 2B). STRING also clustered in this network a group of cytochrome P450 (Cyp) proteins, which were more abundant in Nrf2-KO organoids. As AhR is a major transcriptional regulator of the Cyp family of enzymes (Androutsopoulos et al., 2009), this finding further supports the possibility that Nrf2 deficiency promotes AhR binding to its cognate promoter sequences. As expected, proteins involved in glutathione metabolism were much more abundant in Keap1-KD samples (Figure S3A). Moreover, proteins involved in glycolysis and the PPP were also significantly changed in expression (Figure 3A), although not in a coordinated fashion. Extracellular matrix proteins were much more abundant in organoid preparations from Nrf2-KO than Keap1-KD mice (Figure S3B). Finally, a group of DNA replication and repair proteins were modestly more abundant in Keap1-KD than Nrf2-KO (Figure S3C) organoids.

The effects of Nrf2 on the levels of enzymes involved in glycolysis were also apparent at the metabolic level. LC-MS of metabolites in colon tissue extracts showed dramatic changes in glycolysis, especially in Keap1-KD mice. Metabolic changes included glucose 6-phosphate (Figure 3C) and fructose 6-phosphate (Figure 3D), involved in the first steps of the pathway, which were significantly higher in colons of Keap1-KD mice compared with WT, whereas metabolites such as dihydroxyacetone phosphate (Figure 3E) and glyceraldehyde 3-phosphate (Figure 3F), involved in the later steps of glycolysis, were lower than in WT. These results are consistent with previously reported metabolic flux analyses using $[1,2-^{13}C_2]$ glucose-containing medium in MEF cells, where glucose oxidation and entry of oxaloacetate and acetyl-CoA into the tricarboxylic acid (TCA) cycle were found to be significantly reduced in Nrf2-KO compared with WT cells, whereas Keap1-knockout cells showed a significant increase in substrate entry into the TCA cycle (Singh et al., 2013).

In addition to glycolysis and the PPP, gluconeogenesis also affects the levels of glucose 6-phosphate. Examination of our proteomics data for gluconeogenesis-related enzymes did not reveal any consistent differences among the genotypes, with the exception of hexokinase 1 (Hk1) and glycerol-3-phosphate dehydrogenase 2 (Gpd2), which were significantly differentially abundant in organoids; Hk1 was also approaching significance in liver samples (Table S3 and Figures S4A and S4B). These results are in agreement with the similar hepatic expression of the key gluconeogenic enzymes phosphoenolpyruvate carboxykinase 1 (Pepck) and glucose-6-phosphatase (G6pase) in WT and Keap1-KD mice fed standard diet, and comparable glucose production upon induction of gluconeogenesis in primary hepatocytes from these mice (Slocum et al., 2016). Notably, however, under conditions of high-fat-diet feeding, the expression of both Pepck and G6pase was ~30% lower in Keap1-KD compared with WT mice, suggesting Nrf2-mediated repression of gluconeogenesis (Slocum et al., 2016).

A Liver

Carboxylesterase type B
& UDP-glycosyltransferase family

B Intestinal Organoids

Steroid hormone biosynthesis and
arachidonic acid metabolism (edited*)

log₂ Nrf2 KO/Keap1 KD

Less abundant <-5 —— >5 More abundant

-5   0   +5

Figure 2. Clusters of Metabolic Proteins Identified by STRING Functional Group Enrichment Analyses

(A and B) Network of proteins identified by STRING with both functional enrichments and quantitative relationships in mitochondria-enriched preparations from livers (A) and early-passage intestinal organoids (B) from Nrf2-knockout (Nrf2-KO) and Keap1-knockdown (Keap1-KD) mice. Networks created by STRING "Proteins with values/ranks" tool (Szklarczyk et al., 2019) were rendered in Cytoscape (Shannon et al., 2003) to overlay ratio values (colors). Gray proteins were not identified in the experiments but were included by STRING. For edges, a minimum interaction score of 0.4 (medium confidence) was applied, with disconnected nodes and subnetworks hidden. Some node positions have been adjusted in highly interacting regions to show names. This type of analysis identified clusters of metabolic proteins within the Ces1 and Ugt families in livers (A) and proteins within the Ces1 and Cyp families in intestinal organoids (B) as statistically significantly different between the Nrf2-KO and Keap1-KD genotypes. For other protein clusters, see Figures 3, S2, and S3.

Nrf2 Regulates Gene Expression of Carboxylesterase 1 (Ces1) and Acyl-CoA Oxidase 2 (Acox2)

As the proteomic analyses identified several members of the carboxylesterase 1 (Ces1) family as some of the most statistically significant differentially abundant proteins among the three genotypes in both experimental systems, further investigations were conducted to validate the link. First, mRNA levels for Ces1g were found to be 47-fold higher in Keap1-KD than in WT organoids and 98% lower in Nrf2-KO than in WT organoids (Figure 4A). Second, when intestinal organoids from the three genotypes of mice were treated with a tricyclic cyanoenone (TBE-31, Figure S5A), a compound that reacts with cysteine 151 in Keap1, thereby activating Nrf2 (Dayalan Naidu et al., 2018), the pattern of expression of Ces1g was similar to that of classical Nrf2-target genes, such as Nqo1, Gstp1, and Gclc in early-passage (p3) cultures. Thus, TBE-31 induced Ces1g to high levels in WT (Figure 4B), but not Nrf2-KO organoids (Figure S5B), and its induction was greatly diminished in their Keap1-KD counterparts (Figure S5C). Third, in colon tissue from mice of the three genotypes, mRNA levels for Ces1g and Ces1f were 9- and 1.5-fold, respectively, higher in colon tissue from Keap1-KD mice in comparison with their WT counterparts, whereas these levels were 94% and 80% lower in colons of Nrf2-KO mice, again with a pattern among the genotypes typical of classical Nrf2-target genes (Figure 4C). In addition to changes in mRNA levels, protein levels of Ces1g were similarly affected by genetic disruption or activation of Nrf2 in colon tissues (Figure 4D). Furthermore, the pentacyclic cyanoenone RTA-408 (Figure S5A), which, like TBE-31, reacts with cysteine 151 in Keap1 to activate Nrf2 (Shekh-Ahmad et al., 2018), induced expression of Ces1g and Ces1f dose dependently in colons of WT mice (Figure 4E), in a way similar to that of classical Nrf2-target genes Nqo1 (Figure S5D) and Gclc (Figure S5E).

As in mouse cells and tissues, treatment with TBE-31 or the naturally occurring Nrf2 activator sulforaphane (SFN) upregulated the expression of CES1 in the human hepatoma cell line HepG2, which has high basal levels of CES1 (Figure S6A), in a manner resembling that of NQO1 (Figure S6B) and GCLC (Figure S6C). Silencing of Nrf2 (by RNAi–for *NFE2L2*) (Figure S6D) reduced the expression of CES1 by 35%–40% in
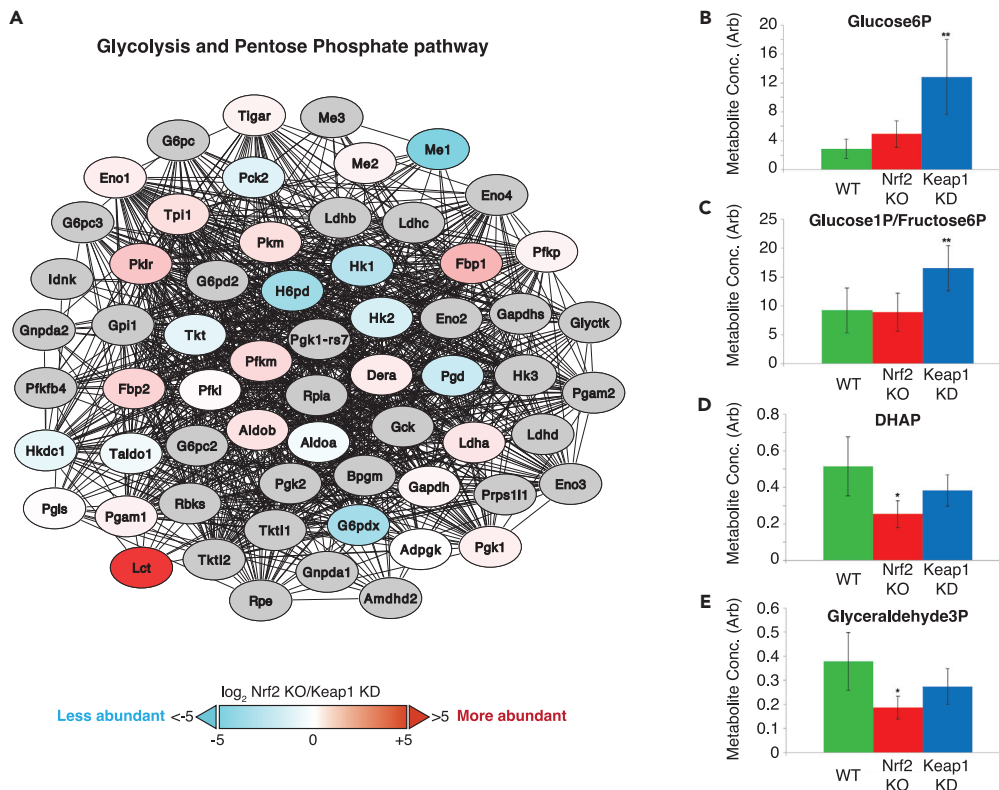
Figure 3. Genetic Interference with Keap1/Nrf2 Affects the Abundance of Glycolytic Enzymes and Metabolites

(A–E) (A) Networks created by STRING "Proteins with values/ranks" tool (Szklarczyk et al., 2019) were rendered in Cytoscape (Shannon et al., 2003) to overlay ratio values (colors). Gray proteins were not identified in the experiments but were included by STRING. For edges, a minimum interaction score of 0.4 (medium confidence) was applied, with disconnected nodes and subnetworks hidden. Some node positions have been adjusted in highly interacting regions to show names. *Edited networks have had proteins not identified in the proteomics analysis removed for brevity. Full details of STRING data can be found in Data S2. In addition to clusters of proteins shown in Figures 2B and S3, this type of analysis identified clusters of proteins involved in glycolysis and the pentose phosphate pathway as statistically significantly different between the Nrf2-KO and Keap1-KD genotypes of organoid preparations. (B–E) Concentration of glucose-6-phosphate (B), glucose-1-phosphate/fructose-6-phosphate (C), dihydroxyacetone phosphate (DHAP) (D), and glyceraldehyde 3-phosphate (E) in colon tissue of C57BL/6 mice. Green bars represent wild-type (WT) mice, red bars Nrf2-knockout (Nrf2-KO) mice, and blue bars Keap1-knockdown (Keap1-KD) mice. * $0.05 > p > 0.01$; ** $0.01 > p > 0.001$. See also Figure S4 and Table S3.

HepG2 cells growing in either glucose-containing or glucose-free medium, and abolished CES1 upregulation by TBE-31 (Figure S6E). The Nrf2 dependence of the expression of CES1 was further confirmed by using the human colorectal cancer cell line DLD1 and its Nrf2-KO and Nrf2-gain-of-function mutant isogenic lines that were generated using CRISPR/Cas9 genome editing (Torrente et al., 2017): compared with Nrf2-WT, the mRNA levels for CES1 were 8.4-fold higher in Nrf2-gain-of-function DLD1 cells, whereas these levels were 75% lower in their Nrf2-KO counterparts (Figure S6F). In Nrf2-WT DLD1 cells, exposure to TBE-31 caused a concentration-dependent Nrf2 stabilization (Figure S6G, immunoblot), and a corresponding CES1 upregulation, which was also observed following treatment with SFN (Figure S6G, bar graph), whereas CES1 upregulation by TBE-31 was greatly diminished in Nrf2-KO DLD1 cells (Figure S6H). Thus, using proteomic, genetic, and pharmacologic approaches, we validated that genes encoding Ces1 family members are transcriptional targets of Nrf2 in human cell lines, in mouse intestinal organoid cultures, and *in vivo* in the murine colon.

Proteomic analysis of mitochondria-enriched preparations isolated from intestinal organoids of WT, Nrf2-KO, and Keap1-KD mice identified another differentially abundant protein of relevance to FAO, namely, acyl-CoA oxidase 2 (Acox2) (Figure 1E), a peroxisomal enzyme that catalyzes oxidation of CoA esters of branched-chain fatty acids and bile acid intermediates (Vanhove et al., 1993). Similar to the classical Nrf2
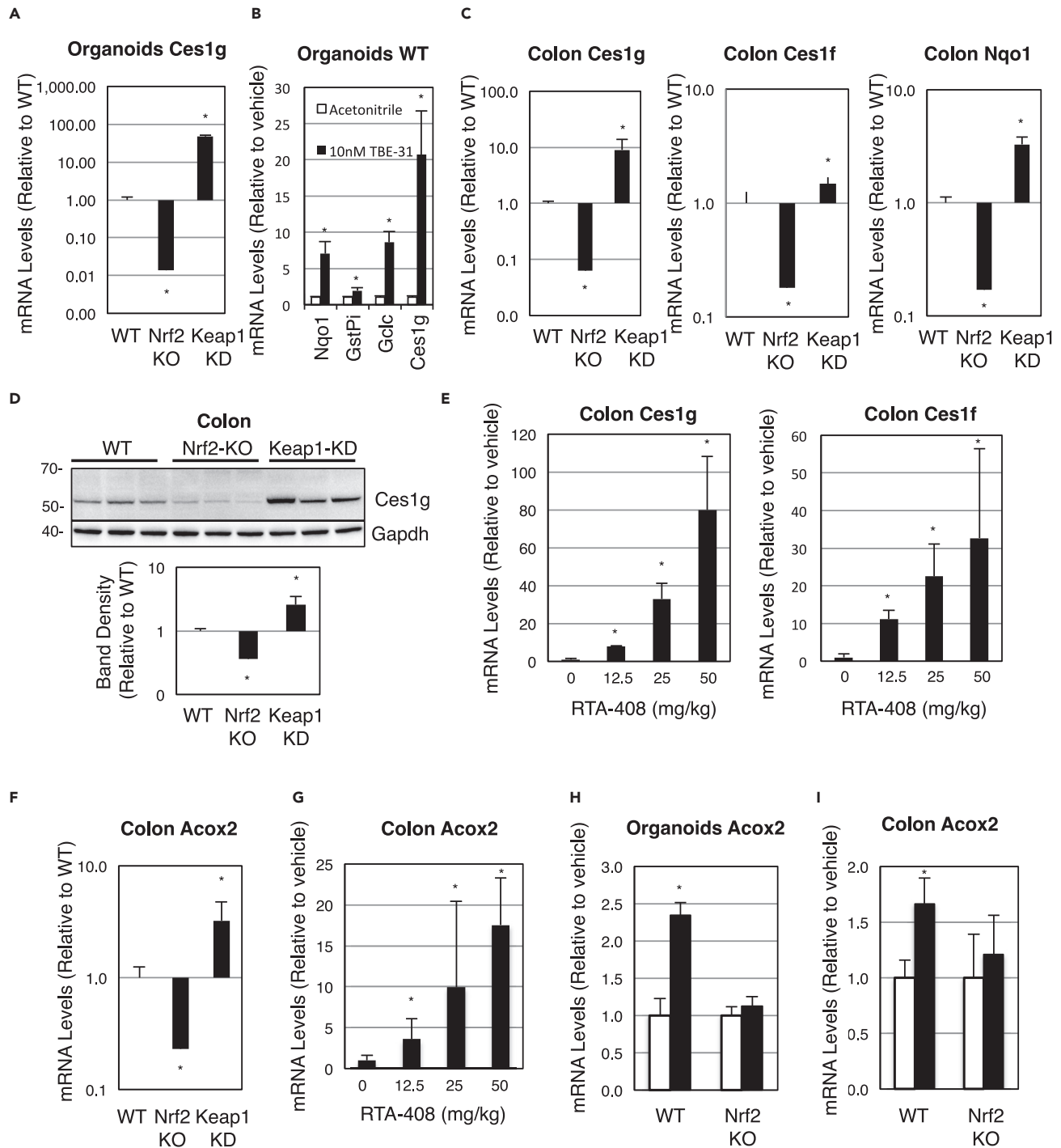
Figure 4. Ces1 and Acox2 Are Transcriptional Targets of Nrf2

(A) mRNA levels for Ces1g in cultures (n = 3) of intestinal organoids from wild-type (WT), Nrf2-knockout (Nrf2-KO), and Keap1-knockdown (Keap1-KD) C57BL/6 mice.

(B) mRNA levels for Nqo1, Gstp, Gclc, and Ces1g in cultures (n = 3) of intestinal organoids from WT C57BL/6 mice that had been treated with vehicle (0.1% acetonitrile) or TBE-31 (10 nM) for 16 h.

(C) mRNA levels for Ces1g, Ces1f, and Nqo1 in colon tissue of WT, Nrf2-KO, and Keap1-KD C57BL/6 mice (n = 3).

(D) Protein levels for Ces1g in colon tissue of WT, Nrf2-KO, and Keap1-KD C57BL/6 mice (n = 3).

Figure 4. Continued

(E) mRNA levels for Ces1g in colon tissue of male C57BL/6 WT mice (n = 3–4) that had been treated with vehicle (1% DMSO in corn oil) or RTA-408, *per os*, 3 times, 24 h apart; colon tissue was harvested 6 h after the last dose.

(F) mRNA levels for Acox2 in colon tissue of WT, Nrf2-KO, and Keap1-KD C57BL/6 mice (n = 5).

(G) mRNA levels for Acox2 in colon tissue of male WT C57BL/6 mice (n = 3–4) that had been treated with vehicle (1% DMSO in corn oil) or RTA-408, *per os*, 3 times, 24 h apart; colon tissue was harvested 6 h after the last dose.

(H) mRNA levels for Acox2 in cultured intestinal organoids (n = 3) from WT and Nrf2-KO C57BL/6 mice that had been treated with vehicle (0.1% acetonitrile, white bars) or TBE-31 (10 nM, black bars) for 16 h.

(I) mRNA levels for Acox2 in the colon of female WT and Nrf2-KO C57BL/6 mice (n = 4–5). The animals were treated with TBE-31 (5 nmol/g body weight, 3 times, at 24-h intervals, *per os,* black bars) or vehicle (1% DMSO in corn oil, white bars) and fasted for 4 h before tissue harvesting 24 h after the last dose. *$p < 0.05$.

See also Figures S5, S6, S7, and S11.

target Nqo1, mRNA levels for Acox2 were 3-fold higher than WT in colons of Keap1-KD, whereas those levels were 80% lower in colons of Nrf2-KO mice (Figure 4F). Oral administration of Nrf2 activator RTA-408 dose dependently induced gene expression of Acox2 in colons of WT animals (Figure 4G), similarly to Ces1g, Ces1f (Figure 4E), Nqo1 (Figure S5D), and Gclc (Figure S5E). In addition, Nrf2 activator TBE-31 induced expression of Acox2 in intestinal organoids from WT, but not Nrf2-KO mice (Figure 4H), in a manner similar to that of Nqo1, Gstp, Gclc, and Ces1g (Figures 4B and S5B). Both Acox2 (Figure 4I) and Nqo1 (Figure S5F) were induced by oral administration of TBE-31 in colons of WT, but not Nrf2-KO mice. Thus, as with Ces1, using both genetic and pharmacologic approaches, we validated that Acox2 is a transcriptional target of Nrf2 in intestinal organoid cultures and *in vivo* in the murine colon.

The levels of ACOX2 have been shown to be downregulated upon knockdown of Nrf2 (by RNAi for *NFE2L2*) in 293T human embryonic fibroblasts (Pang et al., 2014), suggesting that like in mice, human ACOX2 is a transcriptional target of Nrf2. Surprisingly, we found no evidence for Nrf2 dependence of ACOX2 regulation in several human cell lines (i.e., HepG2 [hepatoma], Caco2 [colorectal cancer], and IMR90 [normal lung fibroblasts]) that we tested, and its expression levels were below the limit of detection in DLD1 (colorectal cancer), A549 (lung cancer), and U2OS (osteosarcoma) cells, indicating cell type and/or species specificity. Thus, ACOX2 expression was not upregulated by treatment with TBE-31 or SFN in HepG2 (Figure S7A), Caco2 (Figure S7B), or IMR90 (Figure S7K) cells. A time course analysis in Caco2 cells showed that the basal mRNA levels for ACOX2 increased ~2-fold at the 48-h time point, but there was no difference between vehicle- and SFN-treated cells (Figure S7E). Furthermore, knockdown of Nrf2 (by RNAi for *NFE2L2*) (Figure S7H) in Caco2 cells did not affect the mRNA levels for ACOX2 (Figure S7J). By contrast, the levels of the Nrf2-targets NQO1 (Figures S6B, S7C, S7F, and S7L) and AKR1B10 (Figures S7D, S7G, and S7M) were upregulated by the inducer and downregulated by the small interfering RNA (Figure S7I) treatments, as expected. Thus, it is unlikely that Nrf2 plays a role in the transcriptional regulation of ACOX2 in humans, indicating species differences.

Downregulation of Keap1 Decreases the Levels of Triglycerides and Alters the Lipidome

In agreement with their function in lipid metabolism and our finding that genes encoding Ces1 and Acox2 are transcriptionally activated by Nrf2, levels of triglycerides were lower in livers (Figure 5A) and colons (Figure 5B) of Keap1-KD compared with WT mice. This is fully consistent with the lower hepatic triglyceride levels in Keap1-KD compared with WT mice that had been fed either regular chow or high-fat diet (Slocum et al., 2016). Notably, however, triglyceride levels in the corresponding tissues of Nrf2-KO mice were not significantly different from either WT or Keap1-KD animals (Figures 5A and 5B), indicating that Ces1 and Acox2 are not the only enzymes responsible for differences in triglycerides among the genotypes.

To better understand how fatty acid metabolism was affected by genotype, as suggested by differential expression of Ces1- and Acox2-encoding genes, fatty acids were esterified, after hydrolysis from lipids, and analyzed using gas chromatography-MS. Distinct fatty acid profiles were apparent for each genotype, with the WT again having a mid-point position between the other two genotypes (Figure 5C). Saturated and mono-unsaturated fatty acids, including C14:0, C14:1n9, and C16:0 were higher in Nrf2-KO mice, whereas polyunsaturated fatty acids, such as C22:5n3, C18:3n6, and C20:5n3, and the odd-chain fatty acid C17:0 were lower in Nrf2-KO mice (Figure 5D).

Reduced Expression of Keap1 Lowers Hepatic Levels of Acetyl-CoA

Metabolomic analysis of colon tissue extracts showed that levels of acetyl-CoA were significantly higher in Nrf2-KO mice than in WT or Keap1-KD animals, whereas levels of phosphoenolpyruvate and fructose bis-
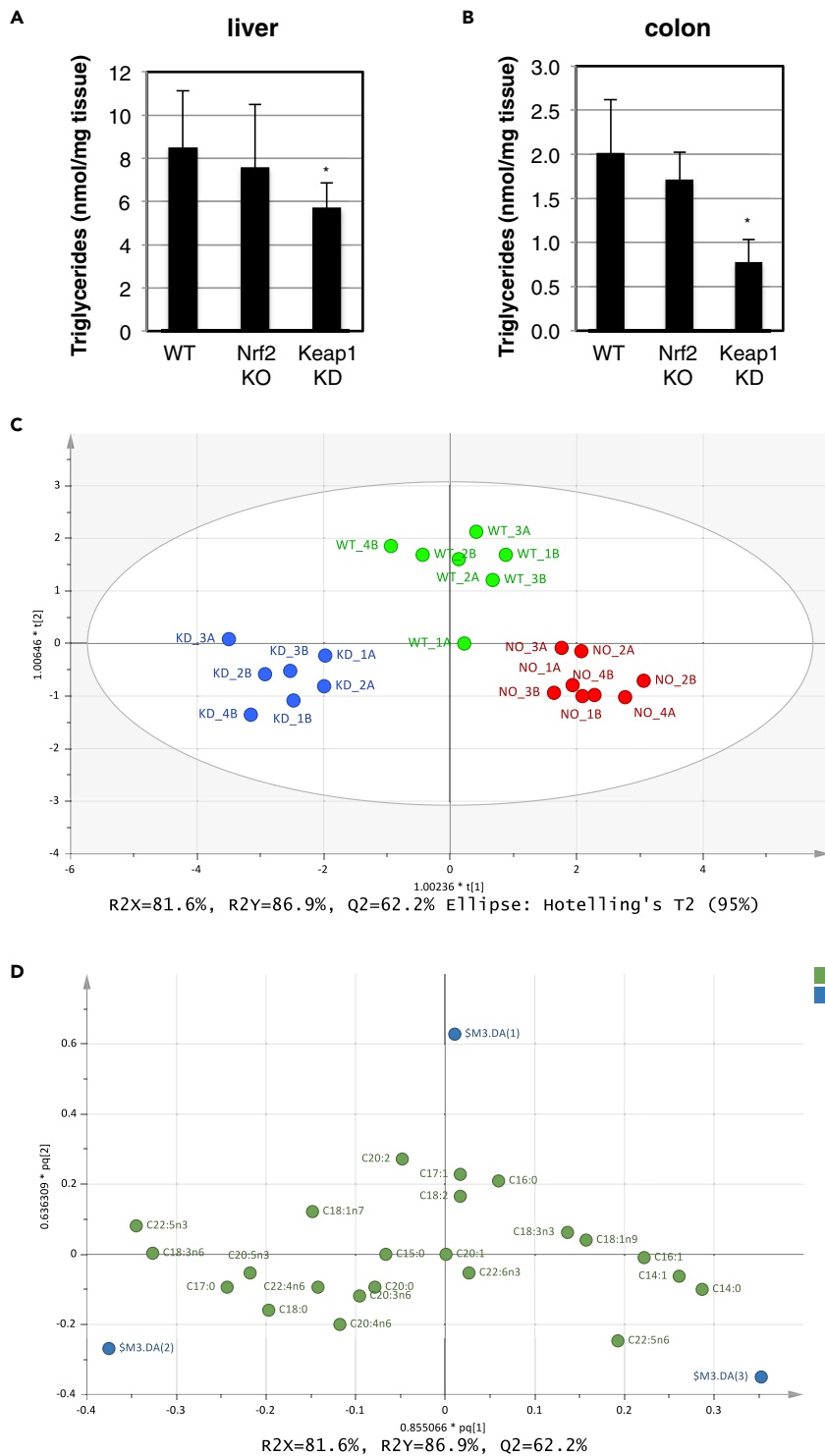
Figure 5. Nrf2 Alters the Lipidome

(A and B) Levels of triglycerides in liver (A) and colon (B) of wild-type (WT), Nrf2-knockout (Nrf2-KO), and Keap1-knockdown (Keap1-KD) C57BL/6 mice (n = 4). *p < 0.05.

(C) Orthogonal projection to latent structure-discriminant analysis (OPLS-DA) score plot from GC-MS data for total fatty acids. Seven independent biological replicates of colon tissue from WT (green), Keap1-KD (blue), and Nrf2-KO (red) C57BL/6 mice were included.

Figure 5. *Continued*

(D) Plot showing the individual fatty acids driving the separation among the genotypes (loadings). The variables (i.e., fatty acids) are represented as green circles, while the direction of the discriminate variable from the classification matrix for each genotype (WT $M1-DA(1), Keap1-KD -$M1-DA(2), and Nrf2-KO $M1-DA(3)) is in blue.

phosphate did not differ among the genotypes (Figure 6A). The enzyme primarily responsible for the synthesis of cytosolic acetyl-CoA is ATP-citrate lyase (Acly). Correlating with differences in acetyl-CoA levels, mRNA levels for Acly were higher in organoid preparations from Nrf2-KO mice compared with their WT or Keap1-KD counterparts (Figure 6B). These differences between WT and Nrf2-KO genotypes are consistent with previous gene expression profiling and proteomics studies demonstrating that Nrf2 negatively regulates the gene expression of Acly in murine liver (Kitteringham et al., 2010; Yates et al., 2009). However, differences in abundance of Acly among the three genotypes were not apparent in our proteomics analysis. To address the possibility that high inter-individual variability may have masked differences in Acly expression among the genotypes, we first examined mRNA levels for Acly in the liver of *ad libitum*-fed WT and Keap1-KD mice. Based on the greater physiological relevance of Keap1 downregulation as opposed to Nrf2 absence, we focused our comparisons on the Keap1-KD and WT genotypes. Indeed, hepatic Acly mRNA levels of *ad libitum*-fed WT mice were highly variable among individual animals (n = 8), although these levels appeared lower in Keap1-KD compared with WT animals (Figures 6C and S8A). We hypothesized that the high inter-individual variability might be due to differences in feeding times, fasted the animals overnight, and found a dramatically decreased (by ∼80%), but much more uniform, hepatic Acly expression (Figure 6C). Levels of Acly mRNA in colon were similar in fed Keap1-KD and WT mice (Figures 6D and S8B), and compared with liver, these levels decreased much more modestly (by ∼20%) following fasting in WT mice, and did not change in KD animals (Figure 6D). Thus, high inter-individual variability and tissue specificity in Acly expression in fed animals provides one explanation for lack of statistically significant differences among the genotypes in our proteomics analysis.

Immunoblotting analysis of hepatic protein levels of Acly in individual mice further revealed that overall, Acly levels were lower in Keap1-KD compared with WT mice at both fed and fasted states (Figure 6E). Furthermore, levels of the Acly reaction product, acetyl-CoA, were lower in livers of *ad libitum*-fed Keap1-KD mice than in WT animals (Figures 6F and S8C). The levels of acetyl-CoA are also affected by the activity of acyl-CoA synthetase short-chain family member 2 (Acss2), which catalyzes the synthesis of acetyl-CoA from acetate (Berg, 1956). Similar to Acly, fasting caused a drop (by ∼80%) in the mRNA levels for Acss2, but in contrast to the lower expression of Acly in livers of fasted Keap1-KD compared with WT mice (Figure 6C), there was no difference in expression of Acss2 between genotypes at either fed or fasted state (Figure S8D). Curiously, the decrease in hepatic protein levels of Acly in fasted mice seemed to correlate with the order of tissue harvest/time after food withdrawal (Figure S8E). As expected, overnight fasting induced expression of a number of classical FAO enzymes, i.e., Cpt1, Cd36, Acads, Acadm, Acadl, and Acadvl, but interestingly, the extent of upregulation was blunted in livers of Keap1-KD animals compared with their WT counterparts (Figure S9A). By contrast, the levels of most enzymes involved in fatty acid synthesis (FAS), i.e., Acaca, Fasn, Scd1, Scd2, Elovl1, and Elovl6, were downregulated by fasting with no difference between genotypes (Figure S9B). In colon, fasting-mediated changes in expression of the classical enzymes involved in FAO and FAS were modest and similar between WT and Keap1-KD animals (Figures S10A and S10B). Notably, the levels of Ces1g and Acox2 were higher in livers and colons of Keap1-KD than WT mice at both fed and fasted states (Figures S11A and S11B).

Collectively, these results show that changes in Acly expression consequent to genetic interference with Keap1/Nrf2 are tissue specific as well as dependent on the nutrient intake (fed versus fasted) state of the animals. In a fed state, acetyl-CoA is directed out of mitochondria to the cytoplasm for use in FAS, whereas under fasted state, acetyl-CoA is channeled into mitochondria for ATP synthesis (Shi and Tu, 2015). Thus, the finding that hepatic levels of acetyl-CoA are lower in fed Keap1-KD compared with WT mice, together with our earlier observations of increased FAO upon Nrf2 activation (Ludtmann et al., 2014) suggest that Nrf2 activation by Keap1 downregulation under fed conditions has features of a fasted metabolic state.

A decrease in acetyl-CoA levels is a trigger for autophagy (Marino et al., 2014). During autophagy, the levels of acetylated (AcK40)-α-tubulin increase, and this event is an essential requirement for starvation-induced autophagy (Geeraert et al., 2010; Marino et al., 2014). We found that levels of acetylated (AcK40)-α-tubulin were higher in hepatic tissue of both *ad libitum*-fed and fasted Keap1-KD mice than in their WT
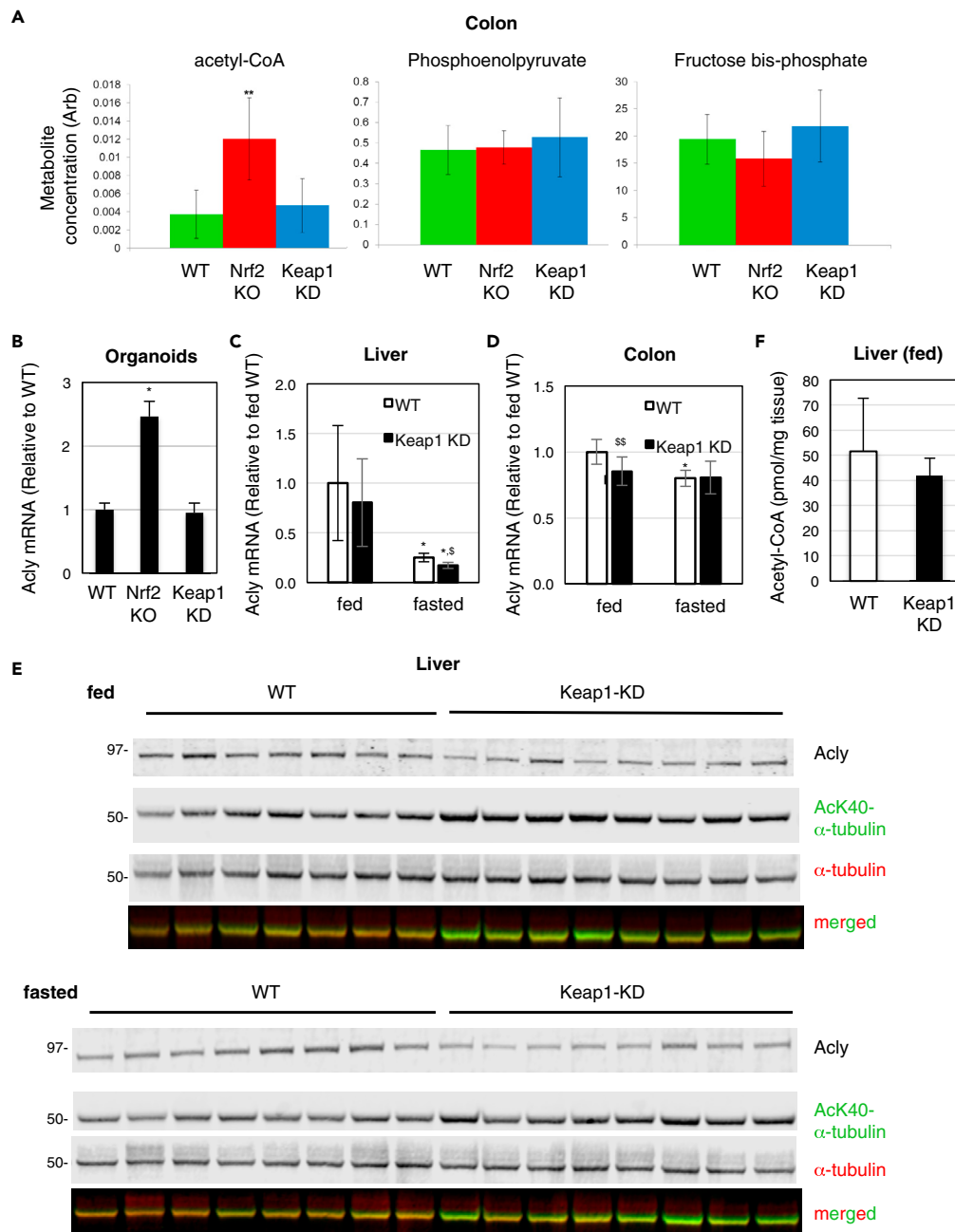
Figure 6. Downregulation of Keap1 Decreases the Hepatic Levels of Acetyl-CoA at Fed State and Increases the Acetylation of α-tubulin Following Fasting

(A) Concentration of phosphoenolpyruvate, fructose bis-phosphate, and acetyl-CoA in colons of wild-type (WT, green bars), Nrf2-knockout (Nrf2-KO, red bars), and Keap1-knockdown (Keap1-KD, blue bars) C57BL/6 mice. ** $0.01 > p > 0.001$.

(B) mRNA levels for Acly in organoids from wild-type (WT), Nrf2-knockout (Nrf2-KO), and Keap1-knockdown (Keap1-KD) C57BL/6 mice. *$p < 0.01$.

(C and D) mRNA levels for Acly in livers (C) and colons (D) of wild-type (WT) and Keap1-knockdown (Keap1-KD) female C57BL/6 mice (n = 8) that were either fed *ad libitum* or fasted for 18 h; *18S* used as a reference gene; *$p < 0.01$, in relation to fed state in respective genotype; $^\$p < 0.01$ and $^{\$\$}0.01 < p < 0.05$, relative to respective WT.

(E) Protein levels for Acly, AcK40-α-tubulin, and α-tubulin in livers from wild-type (WT) and Keap1-knockdown (Keap1-KD) female C57BL/6 mice (n = 7–8) that were either fed *ad libitum* or fasted for 18 h.

(F) Levels of acetyl-CoA in livers of fed wild-type (WT) and Keap1-knockdown (Keap1-KD) female C57BL/6 mice (n = 8). See also Figures S8–S12.

A

B

C
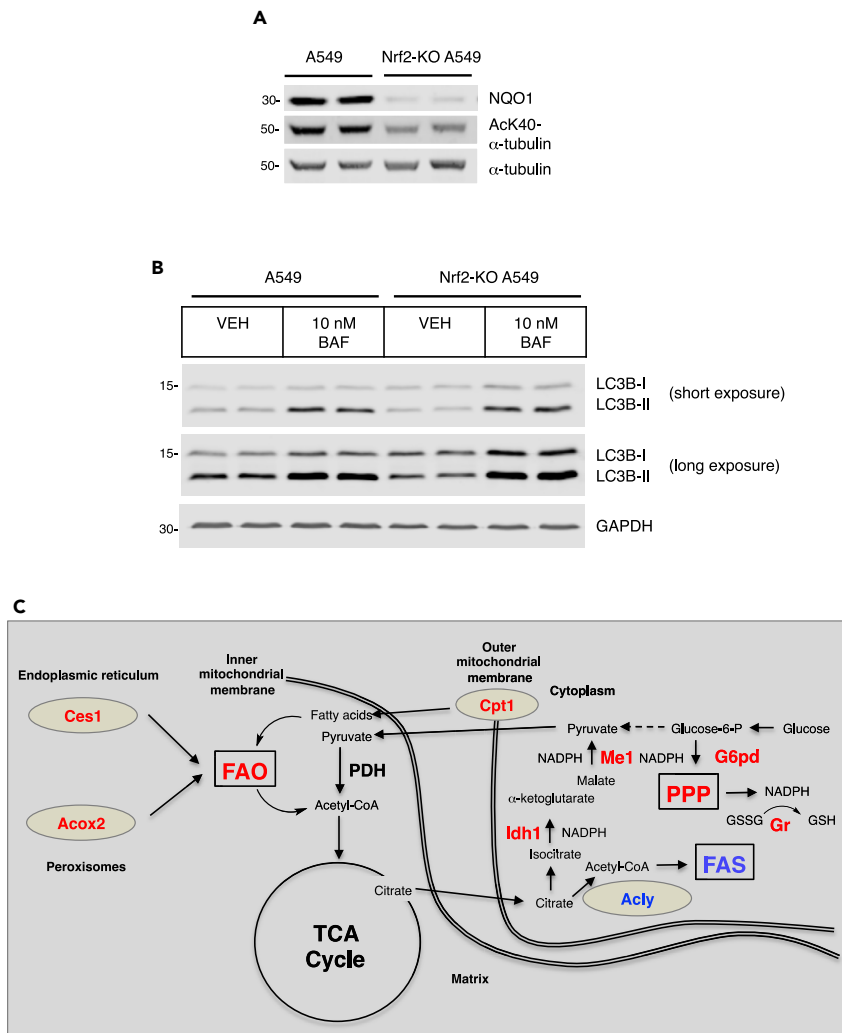
Figure 7. Deletion of Nrf2 in the Context of Mutant Keap1, Which Does Not Suppress Nrf2, Decreases the Acetylation of α-tubulin and Autophagic Flux

(A) Levels of NQO1, AcK40-α-tubulin, and α-tubulin in whole-cell lysates of A549 and Nrf2-KO A549 cells.

(B) Levels of LC3B-I (non-lipidated form) and LC3B-II (lipidated form) in whole-cell lysates of A549 and Nrf2-KO A549 cells that had been treated with vehicle (0.1% DMSO, VEH) or 10 nM bafilomycin A1 (BAF) for 16 h. GAPDH served as a loading control. See also Figure S12.

(C) Downregulation of Keap1 has features of a fasted metabolic state. Nrf2 channels glucose through the pentose phosphate pathway by upregulating glucose-6-phosphate dehydrogenase (G6pd) and the enzymes of the pentose phosphate pathway (PPP) and enhances fatty acid oxidation (FAO) in part by upregulating Ces1 and Acox2, as well as the fatty acid transporter Cpt1, while inhibiting fatty acid synthesis (FAS) by downregulating Acly, and thus decreasing the levels of cytosolic acetyl-CoA. These features of a fasted metabolic state channel acetyl-CoA into the mitochondria for ATP synthesis and increase autophagic flux. The upregulation of the PPP, isocitrate dehydrogenase-1 (Idh1), and malic enzyme-1 (Me1) provides reducing equivalents (NADPH) for redox reactions and regeneration of reduced glutathione (GSH), which is catalyzed by the Nrf2-target enzyme glutathione reductase (Gr).

counterparts (Figures 6E and S8F). Consistent with Nrf2 activation promoting α-tubulin acetylation, compared with WT, the levels of (AcK40)-α-tubulin were higher in primary embryonic fibroblast (MEF) cells isolated from Keap1-KD mice, and lower in their Nrf2-KO counterparts (Figure S12). In close agreement with the mouse data, the levels of (AcK40)-α-tubulin were also higher in human lung cancer A549 cells when compared with CRISPR/Cas9-generated Nrf2-KO A549 cells (Figure 7A). The A549 cell line has consti-tutively high Nrf2 levels due to a homozygous mutation (G333C) in the Kelch domain of Keap1, the site of interaction between Keap1 and Nrf2 (Singh et al., 2006). As this experimental system (i.e., Nrf2-KO A549

and A549 cells) represents the two extreme conditions, namely, Nrf2 absence versus Nrf2 constitutive activation, we used it to examine autophagic flux. We found that, compared with Nrf2-KO A549 cells, autophagic flux was enhanced in the parental A549 cells, as evident by the higher levels of the lipidated form of the autophagosomal marker microtubule-associated protein 1A/1B light chain 3B (LC3B), (LC3B-II), and its further accumulation upon treatment with the autophagy inhibitor bafilomycin A1 (Figure 7B). This result is in agreement with the known involvement of Nrf2 in regulation of multiple genes that participate in macropautophagy and chaperone-mediated autophagy (Pajares et al., 2016, 2018).

DISCUSSION

The results from this study are in agreement with previous reports showing (1) dysregulated expression of lipid-metabolizing enzymes, including lower levels of Ces1g in livers of Nrf2-KO compared with WT mice (Kitteringham et al., 2010; Tanaka et al., 2012); (2) reduced hepatic expression of genes involved in FAS and desaturation in mice with high Nrf2 levels (Sharma et al., 2018; Wu et al., 2011; Yates et al., 2009); (3) increased high-fat-diet-induced levels of lipogenic enzymes in livers of Nrf2-KO compared with WT mice (Meakin et al., 2014); (4) lower ethanol-induced accumulation of free fatty acids in livers of hepatocyte-specific Keap1-knockout mice (Wu et al., 2012); (5) requirement for Nrf2 for hepatic Ces1g induction by the Nrf2 activator oltipraz (Zhang et al., 2012); and (6) higher mRNA levels for Ces1g and Ces1h in lungs of Keap1-knockout compared with WT mice (Paek et al., 2012). Taken together with knowledge that Nrf2 activation in proliferating cells, such as cultured MEF cells, as well as cells in the murine intestinal and forestomach epithelium, channels glucose through the PPP by upregulating glucose-6-phosphate dehydrogenase (G6pd) and enzymes of the PPP (Mitsuishi et al., 2012), our findings suggest that Nrf2 activation confers features of a fasted metabolic state (Figure 7C). Nrf2 activation enhances FAO in part by upregulating Ces1 and Acox2, as well as the uptake of fatty acids through Cd36, while inhibiting FAS by downregulating Acly, and thus decreasing the levels of acetyl-CoA. Notably, however, although Nrf2 activation does not equate typical fasting, the blunted response to fasting of the Keap1-KD mice suggests that Nrf2 activation provides quantitatively modest, but widespread preconditioning to fasting, allowing adaptation to the associated metabolic stress.

Ces1 enzymes catalyze the trans-esterification and hydrolysis of ester, thioester, or amide bonds within various substrates, including acyl glycerols to give free fatty acids and participate in fatty acid and cholesterol ester metabolism (Hosokawa et al., 2007), channeling fatty acids toward oxidation and away from storage (Ko et al., 2009). These enzymes are localized in the ER, which is physically connected with mitochondria (Rowland and Voeltz, 2012). Furthermore, physical contacts between mitochondria and ER lead to formation of specialized structures termed mitochondria-associated membranes, where critical metabolic processes, such as lipid trafficking, reactive oxygen species, and Ca^{2+} signaling occur, thereby allowing localized inter-organellar communication (Csordas et al., 2018; Scorrano et al., 2019). Acting in concert with uridine 5′-diphospho-glucuronosyltransferaseares (UGTs), Ces1 enzymes are also involved in xenobiotic metabolism, including the metabolism of cocaine and heroin and detoxification of organophosphate chemical weapons, such as sarin, soman, and tabun (Bencharit et al., 2003). The UGTs are drug-metabolizing enzymes encoded by classical Nrf2-target genes; indeed, we observed members of this family to be differentially expressed among the genotypes in the proteomics screen (Tables S1 and S2, and Figure 2), confirming the presence of ER proteins in our mitochondria-enriched fractions. Ces1g-knockout mice have reduced energy expenditure, increased lipogenesis, and postprandial hyperlipidemia due to increased secretion of chylomicrons, whereas Ces1g overexpression leads to increased FAO and reduced hepatic triglyceride levels (Quiroga et al., 2012; Xu et al., 2014). Most recently, it was shown that hepatocyte-specific overexpression of human CES1 in mice promotes FAO and attenuates high-fat/high-cholesterol/high-fructose diet- or alcohol-induced hepatic steatosis, inflammation, fibrosis, and hyperlipidemia, strongly suggesting a protective role of hepatic CES1 against metabolic disorders (Xu et al., 2020). Taken together with our findings of the regulation of CES1 by Nrf2, it can be concluded that one mechanism by which Nrf2 activation protects against metabolic disorders is through induction of CES1.

Although other transcription factors are also involved in regulating Ces1 expression, some similarities between Ces1g-KO and Nrf2-KO mice are noteworthy. Thus, Ces1 deficiency results in hepatosteatosis (Quiroga et al., 2012), and albeit to a much lower degree, there is evidence for microvesicular hepatic steatosis in Nrf2-KO animals (Chowdhry et al., 2010; Meakin et al., 2014; Sugimoto et al., 2010). Ces1g-KO mice are protected against development of atherosclerosis (Xu et al., 2017), as are Nrf2-KO mice (Polonen et al., 2019; Sussan et al., 2008). In addition, knockout of Ces1g decreases levels of cholesterol in plasma (Xu et al.,

2017), as does Nrf2 deficiency (Meakin et al., 2014; Polonen et al., 2019), whereas plasma low-density lipoprotein levels are increased following chronic pharmacologic activation of Nrf2 by TBE-31 (Kostov et al., 2015). Taken together, these findings suggest that one mechanism by which Nrf2 activation affects lipid metabolism involves Ces1.

The beneficial effects of intermittent fasting have been consistently observed in numerous preclinical models of chronic disease, including obesity, diabetes, and neurodegenerative diseases, and although the clinical evidence is much more limited, benefits have been also noted in patients with metabolic disorders, such as obesity and insulin resistance (de Cabo and Mattson, 2019). A recent study in mice has shown that although the improvements in physical performance resulting from caloric restriction do not require Nrf2, the alterations in metabolic and protein homeostasis were Nrf2 dependent (Pomatto et al., 2020). Parallels can be drawn between reduced expression of Keap1/activation of Nrf2 and intermittent fasting. Similar to intermittent fasting, Nrf2 activation triggers adaptive responses resulting in improved glucose regulation, increased resistance to stress, and resolution of inflammation. Like Nrf2 activation, which counteracts and provides long-lasting protection against subsequent challenges (Gao et al., 2001), intermittent fasting leads to adaptive responses of long duration, which confer resistance to subsequent potentially damaging exposures and has inspired the search for targeted pharmacologic approaches that mimic the effects of fasting (de Cabo and Mattson, 2019). Our findings suggest that pharmacologic inhibition of Keap1 may offer such approach, particularly for conditions such as obesity-induced metabolic syndrome. Indeed, the anti-inflammatory, anti-lipogenic, and anti-fibrotic effects of Nrf2 pathway activation are particularly pronounced when mice are fed high-fat or high-fat plus high-fructose diet (Meakin et al., 2014; Sharma et al., 2018; Slocum et al., 2016). This notion is further supported by results from a human study showing that a 12-week intervention with the classical Nrf2 activator SFN (administered as broccoli sprout extracts) improved glucose control in obese patients with type 2 diabetes, as evidenced by the decrease in glycated hemoglobin and fasting blood glucose, which correlated with serum SFN concentration (Axelsson et al., 2017). Like TBE-31 and RTA-408, SFN inactivates Keap1 by reacting with cysteine 151 (Zhang and Hannink, 2003).

It should be pointed out that the level of Nrf2 activation in the Keap1-KD animals that we used in this study is relatively modest and comparable to levels observed following interventions with pharmacologic Nrf2 activators in both mice (Knatko et al., 2015) and humans (Dinkova-Kostova et al., 2007; Liu et al., 2020). This was an important consideration, particularly because Nrf2 activators, such as SFN and the pentacyclic cyanoenones bardoxolone methyl and RTA-408 (used in this study), are currently in clinical trials for multiple indications, including chronic kidney disease, liver disease, pulmonary arterial hypertension, mitochondrial myopathy, and autism spectrum disorder (Cuadrado et al., 2019). In addition, development of non-electrophilic compounds, which target the Nrf2-binding domain of Keap1 and consequently disrupt its protein-protein interactions with Nrf2, is also actively being pursued and has been the focus of a recent extensive virtual screen drug discovery effort, in which more than 1 billion compounds were assessed (Gorgulla et al., 2020).

Limitations of the Study

The comparisons among WT, Nrf2-KO, and Keap1-KD genotypes provide confidence that most functional outcomes observed in this study are Nrf2 dependent. Nonetheless, we cannot exclude the possibility that some may be partially Nrf2 dependent. This is because, in addition to activating Nrf2, the lower expression of Keap1 in Keap1-KD animals is expected to affect the behavior of other (known as well as yet to be discovered) Keap1-binding partners, and the potential consequences have not been examined. Another limitation of this study is that, for most experiments, we have used female mice, and although highly unlikely, we cannot exclude the possibility that some of the responses of male mice could be different. Finally, future work is needed to elucidate the mechanisms by which Nrf2 acts as a negative regulator of the proteins identified in our proteomics screen.

Resource Availability

Lead Contact
Albena T. Dinkova-Kostova (a.dinkovakostova@dundee.ac.uk).

Materials Availability
Materials are available from the corresponding author on request.

Data and Code Availability

All data are available in the main text or in Supplemental information and files. The mass spectrometry proteomics data have been deposited to the ProteomeXchange Consortium via the PRIDE partner repository with the dataset identifier PXD021639.

METHODS

All methods can be found in the accompanying Transparent Methods supplemental file.

SUPPLEMENTAL INFORMATION

Supplemental Information can be found online at https://doi.org/10.1016/j.isci.2020.101638.

AUTHOR CONTRIBUTIONS

A.T.D.-K. R.T.H., and J.L.G. conceived the project, designed the experiments, and contributed to data interpretation. A.T.D.-K. wrote the manuscript. E.V.K., Y.Z., M.H.T., C.C., M.H., C.L., and S.D.N. performed biochemical experiments, data analysis and interpretation. M.H.T. performed proteomics experiments, data analysis, and interpretation. C.C. performed lipidomics experiments, data analysis, and interpretation. T.H. synthesized pharmacologic Nrf2 activators. L.d.l.V. produced Nrf2-knockout and Nrf2-gain-of-function DLD1 cell lines, and Nrf2-knockout A549 cells. All authors reviewed and edited the manuscript before submission.

DECLARATION OF INTERESTS

A.T.D.-K. is on the Scientific Advisory Board of Evgen Pharma and is a consultant for Aclipse Therapeutics.

REFERENCES

Androutsopoulos, V.P., Tsatsakis, A.M., and Spandidos, D.A. (2009). Cytochrome P450 CYP1A1: wider roles in cancer progression and prevention. BMC Cancer 9, 187.

Axelsson, A.S., Tubbs, E., Mecham, B., Chacko, S., Nenonen, H.A., Tang, Y., Fahey, J.W., Derry, J.M.J., Wollheim, C.B., Wierup, N., et al. (2017). Sulforaphane reduces hepatic glucose production and improves glucose control in patients with type 2 diabetes. Sci. Transl Med. 9, eaah4477.

Bencharit, S., Morton, C.L., Xue, Y., Potter, P.M., and Redinbo, M.R. (2003). Structural basis of heroin and cocaine metabolism by a promiscuous human drug-processing enzyme. Nat. Struct. Biol. 10, 349–356.

Berg, P. (1956). Acyl adenylates; an enzymatic mechanism of acetate activation. J. Biol. Chem. 222, 991–1013.

Bluher, M. (2019). Obesity: global epidemiology and pathogenesis. Nat. Rev. Endocrinol. 15, 288–298.

Cai, H., Scott, E., Kholghi, A., Andreadi, C., Rufini, A., Karmokar, A., Britton, R.G., Horner-Glister, E., Greaves, P., Jawad, D., et al. (2015). Cancer chemoprevention: evidence of a nonlinear dose response for the protective effects of resveratrol in humans and mice. Sci. Transl Med. 7, 298ra117.

Cho, H.Y., Marzec, J., and Kleeberger, S.R. (2015). Functional polymorphisms in Nrf2: implications for human disease. Free Radic. Biol. Med. 88, 362–372.

Chowdhry, S., Nazmy, M.H., Meakin, P.J., Dinkova-Kostova, A.T., Walsh, S.V., Tsujita, T., Dillon, J.F., Ashford, M.L., and Hayes, J.D. (2010). Loss of Nrf2 markedly exacerbates nonalcoholic steatohepatitis. Free Radic. Biol. Med. 48, 357–371.

Cox, J., and Mann, M. (2008). MaxQuant enables high peptide identification rates, individualized p.p.b.-range mass accuracies and proteome-wide protein quantification. Nat. Biotechnol. 26, 1367–1372.

Csordas, G., Weaver, D., and Hajnoczky, G. (2018). Endoplasmic reticulum-mitochondrial contactology: structure and signaling functions. Trends Cell Biol. 28, 523–540.

Cuadrado, A., Rojo, A.I., Wells, G., Hayes, J.D., Cousin, S.P., Rumsey, W.L., Attucks, O.C., Franklin, S., Levonen, A.L., Kensler, T.W., et al. (2019). Therapeutic targeting of the NRF2 and KEAP1 partnership in chronic diseases. Nat. Rev. Drug Discov. 18, 295–317.

Cullinan, S.B., Gordan, J.D., Jin, J., Harper, J.W., and Diehl, J.A. (2004). The Keap1-BTB protein is an adaptor that bridges Nrf2 to a Cul3-based E3 ligase: oxidative stress sensing by a Cul3-Keap1 ligase. Mol. Cell Biol. 24, 8477–8486.

Dayalan Naidu, S., and Dinkova-Kostova, A.T. (2020). KEAP1, a cysteine-based sensor and a drug target for the prevention and treatment of chronic disease. Open Biol. 10, 200105.

Dayalan Naidu, S., Muramatsu, A., Saito, R., Asami, S., Honda, T., Hosoya, T., Itoh, K., Yamamoto, M., Suzuki, T., and Dinkova-Kostova,

A.T. (2018). C151 in KEAP1 is the main cysteine sensor for the cyanoenone class of NRF2 activators, irrespective of molecular size or shape. Sci. Rep. 8, 8037.

de Cabo, R., and Mattson, M.P. (2019). Effects of intermittent fasting on health, aging, and disease. N. Engl. J. Med. 381, 2541–2551.

Dinkova-Kostova, A.T., Fahey, J.W., Wade, K.L., Jenkins, S.N., Shapiro, T.A., Fuchs, E.J., Kerns, M.L., and Talalay, P. (2007). Induction of the phase 2 response in mouse and human skin by sulforaphane-containing broccoli sprout extracts. Cancer Epidemiol. Biomarkers Prev. 16, 847–851.

Dinkova-Kostova, A.T., Holtzclaw, W.D., Cole, R.N., Itoh, K., Wakabayashi, N., Katoh, Y., Yamamoto, M., and Talalay, P. (2002). Direct evidence that sulfhydryl groups of Keap1 are the sensors regulating induction of phase 2 enzymes that protect against carcinogens and oxidants. Proc. Natl. Acad. Sci. U S A 99, 11908–11913.

Fu, T., Coulter, S., Yoshihara, E., Oh, T.G., Fang, S., Cayabyab, F., Zhu, Q., Zhang, T., Leblanc, M., Liu, S., et al. (2019). FXR regulates intestinal cancer stem cell proliferation. Cell 176, 1098–1112 e1018.

Gao, X., Dinkova-Kostova, A.T., and Talalay, P. (2001). Powerful and prolonged protection of human retinal pigment epithelial cells, keratinocytes, and mouse leukemia cells against oxidative damage: the indirect antioxidant effects of sulforaphane. Proc. Natl. Acad. Sci. U S A 98, 15221–15226.

Geeraert, C., Ratier, A., Pfisterer, S.G., Perdiz, D., Cantaloube, I., Rouault, A., Pattingre, S., Proikas-Cezanne, T., Codogno, P., and Pous, C. (2010). Starvation-induced hyperacetylation of tubulin is required for the stimulation of autophagy by nutrient deprivation. J. Biol. Chem. 285, 24184–24194.

Gorgulla, C., Boeszoermenyi, A., Wang, Z.F., Fischer, P.D., Coote, P.W., Padmanabha Das, K.M., Malets, Y.S., Radchenko, D.S., Moroz, Y.S., Scott, D.A., et al. (2020). An open-source drug discovery platform enables ultra-large virtual screens. Nature 580, 663–668.

Hayes, J.D., and Dinkova-Kostova, A.T. (2014). The Nrf2 regulatory network provides an interface between redox and intermediary metabolism. Trends Biochem. Sci. 39, 199–218.

Hayes, J.D., Dinkova-Kostova, A.T., and McMahon, M. (2009). Cross-talk between transcription factors AhR and Nrf2: lessons for cancer chemoprevention from dioxin. Toxicol. Sci. 111, 199–201.

Holmstrom, K.M., Baird, L., Zhang, Y., Hargreaves, I., Chalasani, A., Land, J.M., Stanyer, L., Yamamoto, M., Dinkova-Kostova, A.T., and Abramov, A.Y. (2013). Nrf2 impacts cellular bioenergetics by controlling substrate availability for mitochondrial respiration. Biol. Open 2, 761–770.

Hosokawa, M., Furihata, T., Yaginuma, Y., Yamamoto, N., Koyano, N., Fujii, A., Nagahara, Y., Satoh, T., and Chiba, K. (2007). Genomic structure and transcriptional regulation of the rat, mouse, and human carboxylesterase genes. Drug Metab. Rev. 39, 1–15.

Kalthoff, S., Ehmer, U., Freiberg, N., Manns, M.P., and Strassburg, C.P. (2010). Interaction between oxidative stress sensor Nrf2 and xenobiotic-activated aryl hydrocarbon receptor in the regulation of the human phase II detoxifying UDP-glucuronosyltransferase 1A10. J. Biol. Chem. 285, 5993–6002.

Kitteringham, N.R., Abdullah, A., Walsh, J., Randle, L., Jenkins, R.E., Sison, R., Goldring, C.E., Powell, H., Sanderson, C., Williams, S., et al. (2010). Proteomic analysis of Nrf2 deficient transgenic mice reveals cellular defence and lipid metabolism as major Nrf2-dependent pathways in the liver. J. Proteomics 73, 1612–1631.

Knatko, E.V., Ibbotson, S.H., Zhang, Y., Higgins, M., Fahey, J.W., Talalay, P., Dawe, R.S., Ferguson, J., Huang, J.T., Clarke, R., et al. (2015). Nrf2 activation protects against solar-simulated ultraviolet radiation in mice and humans. Cancer Prev. Res. (Phila) 8, 475–486.

Ko, K.W., Erickson, B., and Lehner, R. (2009). Es-x/Ces1 prevents triacylglycerol accumulation in McArdle-RH7777 hepatocytes. Biochim. Biophys. Acta 1791, 1133–1143.

Kobayashi, A., Kang, M.I., Okawa, H., Ohtsuji, M., Zenke, Y., Chiba, T., Igarashi, K., and Yamamoto, M. (2004). Oxidative stress sensor Keap1 functions as an adaptor for Cul3-based E3 ligase to regulate proteasomal degradation of Nrf2. Mol. Cell Biol. 24, 7130–7139.

Kostov, R.V., Knatko, E.V., McLaughlin, L.A., Henderson, C.J., Zheng, S., Huang, J.T., Honda, T., and Dinkova-Kostova, A.T. (2015). Pharmacokinetics and pharmacodynamics of orally administered acetylenic tricyclic bis(cyanoenone), a highly potent Nrf2 activator with a reversible covalent mode of action. Biochem. Biophys. Res. Commun. 465, 402–407.

Kuipers, E.J., Grady, W.M., Lieberman, D., Seufferlein, T., Sung, J.J., Boelens, P.G., van de Velde, C.J., and Watanabe, T. (2015). Colorectal cancer. Nat. Rev. Dis. Primers 1, 15065.

Liu, H., Zimmerman, A.W., Singh, K., Connors, S.L., Diggins, E., Stephenson, K.K., Dinkova-Kostova, A.T., and Fahey, J.W. (2020). Biomarker exploration in human peripheral blood mononuclear cells for monitoring sulforaphane treatment responses in autism spectrum disorder. Sci. Rep. 10, 5822.

Ludtmann, M.H., Angelova, P.R., Zhang, Y., Abramov, A.Y., and Dinkova-Kostova, A.T. (2014). Nrf2 affects the efficiency of mitochondrial fatty acid oxidation. Biochem. J. 457, 415–424.

Malhotra, D., Portales-Casamar, E., Singh, A., Srivastava, S., Arenillas, D., Happel, C., Shyr, C., Wakabayashi, N., Kensler, T.W., Wasserman, W.W., et al. (2010). Global mapping of binding sites for Nrf2 identifies novel targets in cell survival response through ChIP-Seq profiling and network analysis. Nucleic Acids Res. 38, 5718–5734.

Marino, G., Pietrocola, F., Eisenberg, T., Kong, Y., Malik, S.A., Andryushkova, A., Schroeder, S., Pendl, T., Harger, A., Niso-Santano, M., et al. (2014). Regulation of autophagy by cytosolic acetyl-coenzyme A. Mol. Cell 53, 710–725.

Meakin, P.J., Chowdhry, S., Sharma, R.S., Ashford, F.B., Walsh, S.V., McCrimmon, R.J., Dinkova-Kostova, A.T., Dillon, J.F., Hayes, J.D., and Ashford, M.L. (2014). Susceptibility of nrf2-null mice to steatohepatitis and cirrhosis upon consumption of a high-fat diet is associated with oxidative stress, perturbation of the unfolded protein response, and disturbance in the expression of metabolic enzymes but not with insulin resistance. Mol. Cell Biol. 34, 3305–3320.

Mitsuishi, Y., Taguchi, K., Kawatani, Y., Shibata, T., Nukiwa, T., Aburatani, H., Yamamoto, M., and Motohashi, H. (2012). Nrf2 redirects glucose and glutamine into anabolic pathways in metabolic reprogramming. Cancer Cell 22, 66–79.

Paek, J., Lo, J.Y., Narasimhan, S.D., Nguyen, T.N., Glover-Cutter, K., Robida-Stubbs, S., Suzuki, T., Yamamoto, M., Blackwell, T.K., and Curran, S.P. (2012). Mitochondrial SKN-1/Nrf mediates a conserved starvation response. Cell Metab. 16, 526–537.

Pajares, M., Jimenez-Moreno, N., Garcia-Yague, A.J., Escoll, M., de Ceballos, M.L., Van Leuven, F., Rabano, A., Yamamoto, M., Rojo, A.I., and Cuadrado, A. (2016). Transcription factor NFE2L2/NRF2 is a regulator of macroautophagy genes. Autophagy 12, 1902–1916.

Pajares, M., Rojo, A.I., Arias, E., Diaz-Carretero, A., Cuervo, A.M., and Cuadrado, A. (2018). Transcription factor NFE2L2/NRF2 modulates chaperone-mediated autophagy through the regulation of LAMP2A. Autophagy 14, 1310–1322.

Pang, S., Lynn, D.A., Lo, J.Y., Paek, J., and Curran, S.P. (2014). SKN-1 and Nrf2 couples proline catabolism with lipid metabolism during nutrient deprivation. Nat. Commun. 5, 5048.

Polonen, P., Jawahar Deen, A., Leinonen, H.M., Jyrkkanen, H.K., Kuosmanen, S., Mononen, M., Jain, A., Tuomainen, T., Pasonen-Seppanen, S., Hartikainen, J.M., et al. (2019). Nrf2 and SQSTM1/p62 jointly contribute to mesenchymal transition and invasion in glioblastoma. Oncogene 38, 7473–7490.

Pomatto, L.C.D., Dill, T., Carboneau, B., Levan, S., Kato, J., Mercken, E.M., Pearson, K.J., Bernier, M., and de Cabo, R. (2020). Deletion of Nrf2 shortens lifespan in C57BL6/J male mice but does not alter the health and survival benefits of caloric restriction. Free Radic. Biol. Med. 152, 650–658.

Quinti, L., Dayalan Naidu, S., Trager, U., Chen, X., Kegel-Gleason, K., Llres, D., Connolly, C., Chopra, V., Low, C., Moniot, S., et al. (2017). KEAP1-modifying small molecule reveals muted NRF2 signaling responses in neural stem cells from Huntington's disease patients. Proc. Natl. Acad. Sci. U S A 114, E4676–E4685.

Quiroga, A.D., Li, L., Trotzmuller, M., Nelson, R., Proctor, S.D., Kofeler, H., and Lehner, R. (2012). Deficiency of carboxylesterase 1/esterase-x results in obesity, hepatic steatosis, and hyperlipidemia. Hepatology 56, 2188–2198.

Rojo de la Vega, M., Chapman, E., and Zhang, D.D. (2018). NRF2 and the hallmarks of cancer. Cancer Cell 34, 21–43.

Rowland, A.A., and Voeltz, G.K. (2012). Endoplasmic reticulum-mitochondria contacts:

function of the junction. Nat. Rev. Mol. Cell Biol. *13*, 607–625.

Scorrano, L., De Matteis, M.A., Emr, S., Giordano, F., Hajnoczky, G., Kornmann, B., Lackner, L.L., Levine, T.P., Pellegrini, L., Reinisch, K., et al. (2019). Coming together to define membrane contact sites. Nat. Commun. *10*, 1287.

Shannon, P., Markiel, A., Ozier, O., Baliga, N.S., Wang, J.T., Ramage, D., Amin, N., Schwikowski, B., and Ideker, T. (2003). Cytoscape: a software environment for integrated models of biomolecular interaction networks. Genome Res. *13*, 2498–2504.

Sharma, R.S., Harrison, D.J., Kisielewski, D., Cassidy, D.M., McNeilly, A.D., Gallagher, J.R., Walsh, S.V., Honda, T., McCrimmon, R.J., Dinkova-Kostova, A.T., et al. (2018). Experimental nonalcoholic steatohepatitis and liver fibrosis are ameliorated by pharmacologic activation of Nrf2 (NF-E2 p45-related factor 2). Cell Mol. Gastroenterol. Hepatol. *5*, 367–398.

Shekh-Ahmad, T., Eckel, R., Dayalan Naidu, S., Higgins, M., Yamamoto, M., Dinkova-Kostova, A.T., Kovac, S., Abramov, A.Y., and Walker, M.C. (2018). KEAP1 inhibition is neuroprotective and suppresses the development of epilepsy. Brain *141*, 1390–1403.

Shi, L., and Tu, B.P. (2015). Acetyl-CoA and the regulation of metabolism: mechanisms and consequences. Curr. Opin. Cell Biol. *33*, 125–131.

Singh, A., Happel, C., Manna, S.K., Acquaah-Mensah, G., Carrerro, J., Kumar, S., Nasipuri, P., Krausz, K.W., Wakabayashi, N., Dewi, R., et al. (2013). Transcription factor NRF2 regulates miR-1 and miR-206 to drive tumorigenesis. J. Clin. Invest. *123*, 2921–2934.

Singh, A., Misra, V., Thimmulappa, R.K., Lee, H., Ames, S., Hoque, M.O., Herman, J.G., Baylin, S.B., Sidransky, D., Gabrielson, E., et al. (2006). Dysfunctional KEAP1-NRF2 interaction in non-small-cell lung cancer. PLoS Med. *3*, e420.

Slocum, S.L., Skoko, J.J., Wakabayashi, N., Aja, S., Yamamoto, M., Kensler, T.W., and Chartoumpekis, D.V. (2016). Keap1/Nrf2 pathway activation leads to a repressed hepatic gluconeogenic and lipogenic program in mice on a high-fat diet. Arch. Biochem. Biophys. *591*, 57–65.

Sugimoto, H., Okada, K., Shoda, J., Warabi, E., Ishige, K., Ueda, T., Taguchi, K., Yanagawa, T., Nakahara, A., Hyodo, I., et al. (2010). Deletion of nuclear factor-E2-related factor-2 leads to rapid onset and progression of nutritional steatohepatitis in mice. Am. J. Physiol. Gastrointest. Liver Physiol. *298*, G283–G294.

Sussan, T.E., Jun, J., Thimmulappa, R., Bedja, D., Antero, M., Gabrielson, K.L., Polotsky, V.Y., and Biswal, S. (2008). Disruption of Nrf2, a key inducer of antioxidant defenses, attenuates ApoE-mediated atherosclerosis in mice. PLoS One *3*, e3791.

Szklarczyk, D., Gable, A.L., Lyon, D., Junge, A., Wyder, S., Huerta-Cepas, J., Simonovic, M., Doncheva, N.T., Morris, J.H., Bork, P., et al. (2019). STRING v11: protein-protein association networks with increased coverage, supporting functional discovery in genome-wide experimental datasets. Nucleic Acids Res. *47*, D607–D613.

Taguchi, K., Maher, J.M., Suzuki, T., Kawatani, Y., Motohashi, H., and Yamamoto, M. (2010). Genetic analysis of cytoprotective functions supported by graded expression of Keap1. Mol. Cell Biol. *30*, 3016–3026.

Tanaka, Y., Ikeda, T., Yamamoto, K., Ogawa, H., and Kamisako, T. (2012). Dysregulated expression of fatty acid oxidation enzymes and iron-regulatory genes in livers of Nrf2-null mice. J. Gastroenterol. Hepatol. *27*, 1711–1717.

Thimmulappa, R.K., Mai, K.H., Srisuma, S., Kensler, T.W., Yamamoto, M., and Biswal, S. (2002). Identification of Nrf2-regulated genes induced by the chemopreventive agent sulforaphane by oligonucleotide microarray. Cancer Res. *62*, 5196–5203.

Torrente, L., Sanchez, C., Moreno, R., Chowdhry, S., Cabello, P., Isono, K., Koseki, H., Honda, T., Hayes, J.D., Dinkova-Kostova, A.T., et al. (2017). Crosstalk between NRF2 and HIPK2 shapes cytoprotective responses. Oncogene *36*, 6204–6212.

Tyanova, S., Temu, T., Sinitcyn, P., Carlson, A., Hein, M.Y., Geiger, T., Mann, M., and Cox, J. (2016). The Perseus computational platform for comprehensive analysis of (prote)omics data. Nat. Methods *13*, 731–740.

Vanhove, G.F., Van Veldhoven, P.P., Fransen, M., Denis, S., Eyssen, H.J., Wanders, R.J., and Mannaerts, G.P. (1993). The CoA esters of 2-methyl-branched chain fatty acids and of the bile acid intermediates di- and trihydroxycoprostanic acids are oxidized by one single peroxisomal branched chain acyl-CoA oxidase in human liver and kidney. J. Biol. Chem. *268*, 10335–10344.

von Otter, M., Landgren, S., Nilsson, S., Celojevic, D., Bergstrom, P., Hakansson, A., Nissbrandt, H., Drozdzik, M., Bialecka, M., Kurzawski, M., et al. (2010). Association of Nrf2-encoding NFE2L2 haplotypes with Parkinson's disease. BMC Med. Genet. *11*, 36.

Wu, K.C., Cui, J.Y., and Klaassen, C.D. (2011). Beneficial role of nrf2 in regulating NADPH generation and consumption. Toxicol. Sci. *123*, 590–600.

Wu, K.C., Liu, J., and Klaassen, C.D. (2012). Role of Nrf2 in preventing ethanol-induced oxidative stress and lipid accumulation. Toxicol. Appl. Pharmacol. *262*, 321–329.

Xu, J., Li, Y., Chen, W.D., Xu, Y., Yin, L., Ge, X., Jadhav, K., Adorini, L., and Zhang, Y. (2014). Hepatic carboxylesterase 1 is essential for both normal and farnesoid X receptor-controlled lipid homeostasis. Hepatology *59*, 1761–1771.

Xu, J., Xu, Y., Xu, Y., Yin, L., and Zhang, Y. (2017). Global inactivation of carboxylesterase 1 (Ces1/Ces1g) protects against atherosclerosis in Ldlr (-/-) mice. Sci. Rep. *7*, 17845.

Xu, Y., Zhu, Y., Bawa, F.C., Hu, S., Pan, X., Yin, L., and Zhang, Y. (2020). Hepatocyte-specific expression of human carboxylesterase 1 attenuates diet-induced steatohepatitis and hyperlipidemia in mice. Hepatol. Commun. *4*, 527–539.

Yamamoto, M., Kensler, T.W., and Motohashi, H. (2018). The KEAP1-NRF2 system: a thiol-based sensor-effector apparatus for maintaining redox homeostasis. Physiol. Rev. *98*, 1169–1203.

Yates, M.S., Tran, Q.T., Dolan, P.M., Osburn, W.O., Shin, S., McCulloch, C.C., Silkworth, J.B., Taguchi, K., Yamamoto, M., Williams, C.R., et al. (2009). Genetic versus chemoprotective activation of Nrf2 signaling: overlapping yet distinct gene expression profiles between Keap1 knockout and triterpenoid-treated mice. Carcinogenesis *30*, 1024–1031.

Yeager, R.L., Reisman, S.A., Aleksunes, L.M., and Klaassen, C.D. (2009). Introducing the "TCDD-inducible AhR-Nrf2 gene battery. Toxicol. Sci. *111*, 238–246.

Zhang, D.D., and Hannink, M. (2003). Distinct cysteine residues in Keap1 are required for Keap1-dependent ubiquitination of Nrf2 and for stabilization of Nrf2 by chemopreventive agents and oxidative stress. Mol. Cell Biol. *23*, 8137–8151.

Zhang, D.D., Lo, S.C., Cross, J.V., Templeton, D.J., and Hannink, M. (2004). Keap1 is a redox-regulated substrate adaptor protein for a Cul3-dependent ubiquitin ligase complex. Mol. Cell Biol. *24*, 10941–10953.

Zhang, Y., Cheng, X., Aleksunes, L., and Klaassen, C.D. (2012). Transcription factor-mediated regulation of carboxylesterase enzymes in livers of mice. Drug Metab. Dispos. *40*, 1191–1197.

Supplemental Information

Downregulation of Keap1 Confers Features

of a Fasted Metabolic State

Elena V. Knatko, Michael H. Tatham, Ying Zhang, Cecilia Castro, Maureen Higgins, Sharadha Dayalan Naidu, Chiara Leonardi, Laureano de la Vega, Tadashi Honda, Julian L. Griffin, Ronald T. Hay, and Albena T. Dinkova-Kostova

Liver

Uniprot Accession	Uniprot Locus	Protein name	Gene name	Average $\log_2$ Nrf2 KO/Keap1 KD	Average -$\log_{10}$ p-value Nrf2 KO v Keap1 KD	T-test Significant Nrf2 KO v Keap1 KD Run 1	T-test Significant Nrf2 KO v Keap1 KD Run 2	$\log_2$ Nrf2/Keap1 Run 1	$\log_2$ Nrf2/Keap1 Run 2	-log p-value Nrf2 KO v Keap1 KD Run 1	-log p-value Nrf2 KO v Keap1 KD Run 2
P48410	ABCD1_MOUSE	ATP-binding cassette sub-family D member 1	Abcd1	-1.79	2.22	+	+	-1.92	-1.66	2.61	1.83
P97449	AMPN_MOUSE	Aminopeptidase N	Anpep	1.64	2.05	+	+	1.38	1.90	2.60	1.51
P16015	CAH3_MOUSE	Carbonic anhydrase 3	Ca3	1.62	2.02	+	+	1.61	1.62	2.12	1.92
P48758	CBR1_MOUSE	Carbonyl reductase [NADPH] 1	Cbr1*	-0.97	2.57	+	+	-0.95	-0.98	2.90	2.25
Q8VCC2	EST1_MOUSE	Liver carboxylesterase 1	Ces1*	-4.09	1.97	+	+	-4.25	-3.92	1.73	2.21
Q8VCT4	CES1D_MOUSE	Carboxylesterase 1D	Ces1d	-0.68	2.63	+	+	-0.58	-0.78	2.73	2.54
H3BL34	H3BL34_MOUSE	Carboxylic ester hydrolase	Ces1e	-1.28	2.01	+	+	-1.41	-1.14	2.04	1.98
Q91WU0	CES1F_MOUSE	Carboxylesterase 1F	Ces1f*	-2.48	3.54	+	+	-2.89	-2.07	4.56	2.51
Q91WG0	EST2C_MOUSE	Acylcarnitine hydrolase	Ces2c	-2.98	1.88	+	+	-2.11	-3.85	1.85	1.90
Q8BJ64	CHDH_MOUSE	Choline dehydrogenase, mitochondrial	Chdh	-0.74	2.67	+	+	-0.76	-0.72	2.76	2.58
O88668	CREG1_MOUSE	Protein CREG1	Creg1*	-1.32	2.75	+	+	-1.36	-1.29	2.50	2.99
P15392	CP2A4_MOUSE	Cytochrome P450 2A4	Cyp2a4	-2.65	2.95	+	+	-2.64	-2.67	3.22	2.69
Q91X75	Q91X75_MOUSE	Cyp2a4 protein	Cyp2a5	-3.89	3.07	+	+	-4.03	-3.74	2.91	3.24
P33267	CP2F2_MOUSE	Cytochrome P450 2F2	Cyp2f2	-1.30	1.96	+	+	-1.40	-1.21	2.01	1.90
Q9WUZ9	ENTP5_MOUSE	Ectonucleoside triphosphate diphosphohydrolase 5	Entpd5	-2.06	3.94	+	+	-2.34	-1.79	3.72	4.17
Q9D379	HYEP_MOUSE	Epoxide hydrolase 1	Ephx1	-2.19	3.30	+	+	-2.41	-1.97	3.77	2.84
E9PV24	FIBA_MOUSE	Fibrinogen alpha chain	Fga	0.88	1.95	+	+	1.00	0.76	2.19	1.70
P15105	GLNA_MOUSE	Glutamine synthetase	Glul	1.08	2.04	+	+	1.04	1.13	2.48	1.60
P10649	GSTM1_MOUSE	Glutathione S-transferase Mu 1	Gstm1*	-3.37	2.93	+	+	-3.36	-3.38	2.66	3.21
Q8CFX1	G6PE_MOUSE	GDH/6PGL endoplasmic bifunctional protein	H6pd*	-0.82	2.39	+	+	-0.75	-0.88	2.43	2.35
Q8VCR2	DHB13_MOUSE	17-beta-hydroxysteroid dehydrogenase 13	Hsd17b13	-6.58	4.22	+	+	-6.95	-6.22	5.52	2.92
Q3U816	Q3U816_MOUSE	Oxidoreductase HTATIP2	Htatip2*	-3.39	4.21	+	+	-4.02	-2.76	4.71	3.71
Q9DCY0	KEG1_MOUSE	Glycine N-acyltransferase-like protein Keg1	Keg1	-1.34	1.97	+	+	-1.39	-1.29	2.15	1.79
Q71RI9	KAT3_MOUSE	Kynurenine--oxoglutarate transaminase 3	Kyat3	-0.84	2.95	+	+	-0.91	-0.77	3.06	2.83
Q7TNG8	LDHD_MOUSE	Probable D-lactate dehydrogenase, mitochondrial	Ldhd	-0.92	2.68	+	+	-1.02	-0.82	3.19	2.17
Q9DBN5	LONP2_MOUSE	Lon protease homolog 2, peroxisomal	Lonp2	-0.78	2.93	+	+	-0.86	-0.71	3.18	2.67
Q3ULD5	MCCB_MOUSE	Methylcrotonoyl-CoA carboxylase beta chain, mitochondrial	Mccc2	-0.56	2.74	+	+	-0.61	-0.50	2.71	2.76
Q8BH59	CMC1_MOUSE	Calcium-binding mitochondrial carrier protein Aralar1	Slc25a12	0.74	2.54	+	+	0.86	0.61	2.68	2.39
K9J7B2	K9J7B2_MOUSE	UDP-glucuronosyltransferase	Ugt1a6b	-1.20	2.20	+	+	-1.30	-1.10	2.30	2.09
Q8R084	Q8R084_MOUSE	UDP-glucuronosyltransferase	Ugt2b1	-1.39	3.66	+	+	-1.50	-1.28	3.15	4.17
Q8BJL9	Q8BJL9_MOUSE	UDP-glucuronosyltransferase	Ugt2b35*	-3.76	3.34	+	+	-3.69	-3.82	2.24	4.45
Q8K169	Q8K169_MOUSE	UDP-glucuronosyltransferase	Ugt2b5	-1.60	3.57	+	+	-1.63	-1.57	3.58	3.55

Table S1. Shortlist of 32 proteins identified as significantly different (FDR 10% & S0=0.1 - See Figure S1) in both MS runs from the liver samples. Student's two tailed t-test results and $\log_2$ Nrf2 KO/Keap1 KD ratios are presented. A negative $\log_2$ ratio is indicative of a protein whose abundance is positively influenced by Nrf2 and/or negatively influenced by Keap1. For further details see Data S1. Proteins organised by gene name. *Proteins also shortlisted from the organoid samples are marked with an asterisk. Related to Figure 1.

Intestinal Organoids

Uniprot Accession	Uniprot Locus	Protein name	Gene name	Average log$_2$ Nrf2 KO/Keap1 KD	Average -log$_{10}$ p-value Nrf2 KO v Keap1 KD	T-test Significant Nrf2 KO v Keap KD Run 1	T-test Significant Nrf2 KO v Keap KD Run 2	log$_2$ Nrf2/Keap 1 Run 1	log$_2$ Nrf2/Keap 1 Run 2	-log p-value Nrf2 KO v Keap1 KD Run 1	-log p-value Nrf2 KO v Keap1 KD Run 2
B2RX12	MRP3_MOUSE	Canalicular multispecific organic anion transporter 2	Abcc3	-2.73	2.46	+	+	-3.08	-2.38	2.63	2.30
E9Q236	E9Q236_MOUSE	ATP-binding cassette, sub-family C (CFTR/MRP), member 4	Abcc4	-3.49	2.91	+	+	-3.01	-3.96	2.54	3.29
Q9QXD1	ACOX2_MOUSE	Peroxisomal acyl-coenzyme A oxidase 2	Acox2	-5.66	3.27	+	+	-5.61	-5.70	2.12	4.42
Q99NF1	BCDO2_MOUSE	Beta,beta-carotene 9,10-oxygenase	Bco2	2.34	2.63	+	+	3.15	1.53	2.95	2.32
P48758	CBR1_MOUSE	Carbonyl reductase [NADPH] 1	Cbr1*	-2.69	3.30	+	+	-2.73	-2.66	3.19	3.42
Q8K354	CBR3_MOUSE	Carbonyl reductase [NADPH] 3	Cbr3	-6.36	3.47	+	+	-6.06	-6.66	3.85	3.08
Q8VCC2	EST1_MOUSE	Liver carboxylesterase 1	Ces1*	-6.41	3.61	+	+	-5.91	-6.91	3.31	3.91
Q91WU0	CES1F_MOUSE	Carboxylesterase 1F	Ces1f*	-6.33	2.56	+	+	-6.70	-5.97	2.83	2.30
O88668	CREG1_MOUSE	Protein CREG1	Creg1*	-1.70	1.93	+	+	-1.64	-1.76	2.06	1.81
Q9WUD0	Q9WUD0_MOUSE	Cytochrome P450 2B10	Cyp2b10	2.40	1.90	+	+	2.39	2.41	2.00	1.81
O88533	DDC_MOUSE	Aromatic-L-amino-acid decarboxylase	Ddc	-3.24	2.29	+	+	-3.44	-3.05	2.31	2.27
Q9D379	HYEP_MOUSE	Epoxide hydrolase 1	Ephx1*	-1.63	2.66	+	+	-1.67	-1.60	2.78	2.54
Q8R180	ERO1A_MOUSE	ERO1-like protein alpha	Ero1a	-2.99	2.65	+	+	-3.21	-2.77	2.77	2.54
Q9D6U8	F162A_MOUSE	Protein FAM162A	Fam162a	-1.59	3.02	+	+	-1.69	-1.50	3.14	2.90
Q00612	G6PD1_MOUSE	Glucose-6-phosphate 1-dehydrogenase X	G6pdx	-2.72	2.99	+	+	-2.83	-2.61	3.31	2.67
P97494	GSH1_MOUSE	Glutamate--cysteine ligase catalytic subunit	Gclc	-4.97	3.29	+	+	-4.41	-5.53	2.84	3.75
O09172	GSH0_MOUSE	Glutamate--cysteine ligase regulatory subunit	Gclm	-2.92	3.28	+	+	-2.86	-2.97	2.90	3.66
Q64521	GPDM_MOUSE	Glycerol-3-phosphate dehydrogenase, mitochondrial	Gpd2	-0.84	2.89	+	+	-0.76	-0.92	2.98	2.81
A0A0R4J111	A0A0R4J111_MOUSE	Glutathione peroxidase	Gpx2	-2.86	2.97	+	+	-2.59	-3.13	3.36	2.58
P47791	GSHR_MOUSE	Glutathione reductase, mitochondrial	Gsr	-2.38	2.89	+	+	-2.44	-2.33	3.56	2.22
P13745	GSTA1_MOUSE	Glutathione S-transferase A1	Gsta1	-5.98	2.86	+	+	-7.23	-4.73	3.89	1.83
P30115	GSTA3_MOUSE	Glutathione S-transferase A3	Gsta3	-5.51	2.68	+	+	-5.91	-5.11	3.14	2.21
Q9DCM2	GSTK1_MOUSE	Glutathione S-transferase kappa 1	Gstk1	-1.04	2.26	+	+	-1.05	-1.03	2.37	2.14
P10649	GSTM1_MOUSE	Glutathione S-transferase Mu 1	Gstm1*	-5.02	3.76	+	+	-5.04	-5.00	3.74	3.78
P19639	GSTM3_MOUSE	Glutathione S-transferase Mu 3	Gstm3	-3.74	3.19	+	+	-3.68	-3.81	3.28	3.10
Q8CFX1	G6PE_MOUSE	GDH/6PGL endoplasmic bifunctional protein	H6pd*	-2.90	2.77	+	+	-2.96	-2.83	2.95	2.59
Q8K2C9	HACD3_MOUSE	Very-long-chain (3R)-3-hydroxyacyl-CoA dehydratase 3	Hacd3	-0.89	2.32	+	+	-0.82	-0.97	2.35	2.28
G3UVV4	G3UVV4_MOUSE	Hexokinase 1, isoform CRA_f	Hk1	-2.15	2.06	+	+	-2.14	-2.17	2.10	2.02
Q3U816	Q3U816_MOUSE	Oxidoreductase HTATIP2	Htatip2*	-2.16	2.80	+	+	-2.23	-2.08	3.78	1.83
F8VPT3	F8VPT3_MOUSE	Lactase	Lct	5.67	1.87	+	+	5.70	5.63	1.88	1.85
P06801	MAOX_MOUSE	NADP-dependent malic enzyme	Me1	-4.13	2.99	+	+	-4.22	-4.04	3.74	2.23
Q91VS7	MGST1_MOUSE	Microsomal glutathione S-transferase 1	Mgst1	-0.99	2.08	+	+	-1.02	-0.97	2.09	2.06
Q7M758	NALDL_MOUSE	Aminopeptidase NAALADL1	Naaladl1	-3.94	2.43	+	+	-4.10	-3.79	3.01	1.85
Q64669	NQO1_MOUSE	NAD(P)H dehydrogenase [quinone] 1	Nqo1	-5.28	3.90	+	+	-5.25	-5.31	4.30	3.49
Q9DCD0	6PGD_MOUSE	6-phosphogluconate dehydrogenase, decarboxylating	Pgd	-1.49	3.19	+	+	-1.62	-1.35	3.05	3.32
Q9D711	PIR_MOUSE	Pirin	Pir	-2.29	1.94	+	+	-2.37	-2.20	2.09	1.79
Q9DBX5	Q9DBX5_MOUSE	Phospholipase A2	Pla2g4a	-1.82	1.87	+	+	-1.59	-2.05	1.83	1.90
Q91YR9	PTGR1_MOUSE	Prostaglandin reductase 1	Ptgr1	-2.97	2.71	+	+	-3.14	-2.79	3.34	2.07
P43137	LIT1_MOUSE	Lithostathine-1	Reg1	3.55	2.50	+	+	3.56	3.54	2.70	2.30
P52760	RIDA_MOUSE	2-iminobutanoate/2-iminopropanoate deaminase	Rida	-4.30	2.98	+	+	-4.16	-4.45	2.80	3.15
Q99P72	RTN4_MOUSE	Reticulon-4	Rtn4	-1.38	2.35	+	+	-1.36	-1.40	2.03	2.67
Q91Y74	SIA4C_MOUSE	CMP-N-acetylneuraminate-beta-galactosamide-alpha-2,3-sialyltransferase 4	St3gal4	6.31	3.90	+	+	6.20	6.43	3.58	4.21
Q9D939	ST1C2_MOUSE	Sulfotransferase 1C2	Sult1c2	2.05	2.48	+	+	1.87	2.23	2.17	2.80
E9Q6Q8	E9Q6Q8_MOUSE	TBC1 domain family member 4	Tbc1d4	-1.55	2.07	+	+	-1.30	-1.80	2.18	1.95
Q9JMH6	TRXR1_MOUSE	Thioredoxin reductase 1, cytoplasmic	Txnrd1	-1.46	2.50	+	+	-1.28	-1.63	2.99	2.00
O70475	UGDH_MOUSE	UDP-glucose 6-dehydrogenase	Ugdh	-3.28	3.40	+	+	-3.32	-3.23	3.59	3.20
Q91ZJ5	Q91ZJ5_MOUSE	UTP--glucose-1-phosphate uridylyltransferase	Ugp2	-2.04	2.31	+	+	-1.82	-2.25	1.82	2.79
Q64435	UD16_MOUSE	UDP-glucuronosyltransferase 1-6	Ugt1a6	-3.37	2.38	+	+	-3.37	-3.36	2.11	2.66
Q8BJL9	Q8BJL9_MOUSE	UDP-glucuronosyltransferase	Ugt2b35*	-2.32	3.57	+	+	-2.44	-2.20	3.99	3.15
Q3UEP4	Q3UEP4_MOUSE	UDP-glucuronosyltransferase	Ugt2b36	-1.99	2.20	+	+	-1.98	-2.00	1.79	2.61

Table S2. Shortlist of 50 proteins identified as significantly different (FDR 10% & S0=0.1 - See Figure S1) in both MS runs from the intestinal organoid samples. Student's two tailed t-test results and log$_2$ Nrf2 KO/Keap1 KD ratios are presented. A negative log$_2$ ratio is indicative of a protein whose abundance is positively influenced by Nrf2 and/or negatively influenced by Keap1. For further details see Data S1. Proteins organised by gene name. *Proteins also shortlisted from the liver samples are marked with an asterisk. Related to Figure 1.

Gene name	Fasta headers	Gluconeogenesis related	Liver_log2 NRF2/KEAP1	Liver_p-value NRF2/KEAP1	Student's T-test Significant Liver	Organoids_log2 NRF2/KEAP1	Organoids_p-value NRF2/KEAP1	Student's T-test Significant Organoids
Aldoa	sp|P05064|ALDOA_MOUSE Fructose-bisphosphate aldo	+	0.21	0.28		-0.31	1.01	
Aldob	sp|Q91Y97|ALDOB_MOUSE Fructose-bisphosphate aldo	+	0.46	0.65		0.68	0.67	
Aldoc	sp|P05063|ALDOC_MOUSE Fructose-bisphosphate aldo	+				0.64	1.23	
Dera	sp|Q91YP3|DEOC_MOUSE Deoxyribose-phosphate aldo	+				0.51	1.42	
Eno1	sp|P17182|ENOA_MOUSE Alpha-enolase OS=Mus mus	+	0.56	0.88		0.46	0.47	
Fbp1	sp|Q9QXD6|F16P1_MOUSE Fructose-1,6-bisphosphatas	+	1.52	1.10		1.77	1.61	
Fbp2	sp|P70695|F16P2_MOUSE Fructose-1,6-bisphosphatase	+				1.05	1.21	
G6pc	sp|P35576|G6PC_MOUSE Glucose-6-phosphatase OS=N	+	1.09	0.65				
Gapdh	sp|P16858|G3P_MOUSE Glyceraldehyde-3-phosphate c	+	0.65	0.61		0.30	1.17	
Got1	sp|P05201|AATC_MOUSE Aspartate aminotransferase,	+	1.14	0.76		1.18	1.11	
Got2	sp|P05202|AATM_MOUSE Aspartate aminotransferase	+	0.29	0.91		-0.33	0.36	
Gpd1	sp|P13707|GPDA_MOUSE Glycerol-3-phosphate dehydr	+	-0.27	1.86		0.77	0.73	
Gpd2	sp|Q64521|GPDM_MOUSE Glycerol-3-phosphate dehyc	+	0.21	0.54		-0.84	2.89	+
Gpi	sp|P06745|G6PI_MOUSE Glucose-6-phosphate isomera	+				0.32	0.25	
Hk1	tr|G3UVV4|G3UVV4_MOUSE Hexokinase 1, isoform CR	+	-1.50	0.66		-2.15	2.06	+
Hk2	sp|O08528|HXK2_MOUSE Hexokinase-2 OS=Mus muscu	+				-1.15	1.60	
Hkdc1	sp|Q91W97|HKDC1_MOUSE Hexokinase HKDC1 OS=Mu	+				-0.66	0.95	
Hoga1	sp|Q9DCU9|HOGA1_MOUSE 4-hydroxy-2-oxoglutarate	+	-0.06	0.12				
Khk	tr|A0A0J9YU79|A0A0J9YU79_MOUSE Ketohexokinase C	+				1.77	1.03	
Mdh1	sp|P14152|MDHC_MOUSE Malate dehydrogenase, cyto	+	-0.09	0.30		0.31	0.51	
Mdh2	sp|P08249|MDHM_MOUSE Malate dehydrogenase, mit	+	-0.11	0.37		-0.09	0.32	
Pck2	sp|Q8BH04|PCKGM_MOUSE Phosphoenolpyruvate carb	+	-1.81	0.29		-0.91	0.52	
Pcx	tr|G5E8R3|G5E8R3_MOUSE Pyruvate carboxylase OS=N	+	-0.49	1.44		-0.95	1.13	
Pgam1	sp|Q9DBJ1|PGAM1_MOUSE Phosphoglycerate mutase	+	1.06	1.16		0.40	0.63	
Pgk1	sp|P09411|PGK1_MOUSE Phosphoglycerate kinase 1 O!	+	0.93	0.61		0.42	0.94	
Pgm1	sp|Q9D0F9|PGM1_MOUSE Phosphoglucomutase-1 OS=	+	1.16	0.89		-1.05	1.84	
Rbp4	sp|Q00724|RET4_MOUSE Retinol-binding protein 4 OS=	+	0.38	0.78				
Slc25a1	sp|Q8JZU2|TXTP_MOUSE Tricarboxylate transport prot	+	-0.18	0.98		-0.51	1.10	
Slc25a10	sp|Q9QZD8|DIC_MOUSE Mitochondrial dicarboxylate ca	+	-0.22	0.82		-0.21	0.61	
Slc25a11	sp|Q9CR62|M2OM_MOUSE Mitochondrial 2-oxoglutara	+	0.15	0.62		0.04	0.03	
Slc25a12	sp|Q8BH59|CMC1_MOUSE Calcium-binding mitochond	+	0.74	2.54		0.08	0.12	
Slc25a13	sp|Q9QXX4|CMC2_MOUSE Calcium-binding mitochond	+	-0.15	0.50		-0.16	0.16	
Slc37a4	tr|Q9D1F9|Q9D1F9_MOUSE Solute carrier family 37 (G	+	-0.32	0.24		1.57	1.25	
Taldo1	sp|Q93092|TALDO_MOUSE Transaldolase OS=Mus mu!	+				-0.41	1.74	
Tpi1	sp|P17751|TPIS_MOUSE Triosephosphate isomerase O	+	0.80	0.40		0.76	0.70	

Table S3. Proteins related to gluconeogenesis that were detected in both MS runs from the liver and organoid samples (see also Figure S4). Student's two tailed t-test was used to determine statistical significance, and log2 Nrf2 KO/Keap1 KD ratios are presented. A negative log2 ratio is indicative of a protein whose abundance is positively influenced by Nrf2 and/or negatively influenced by Keap1. Related to Figure 3.
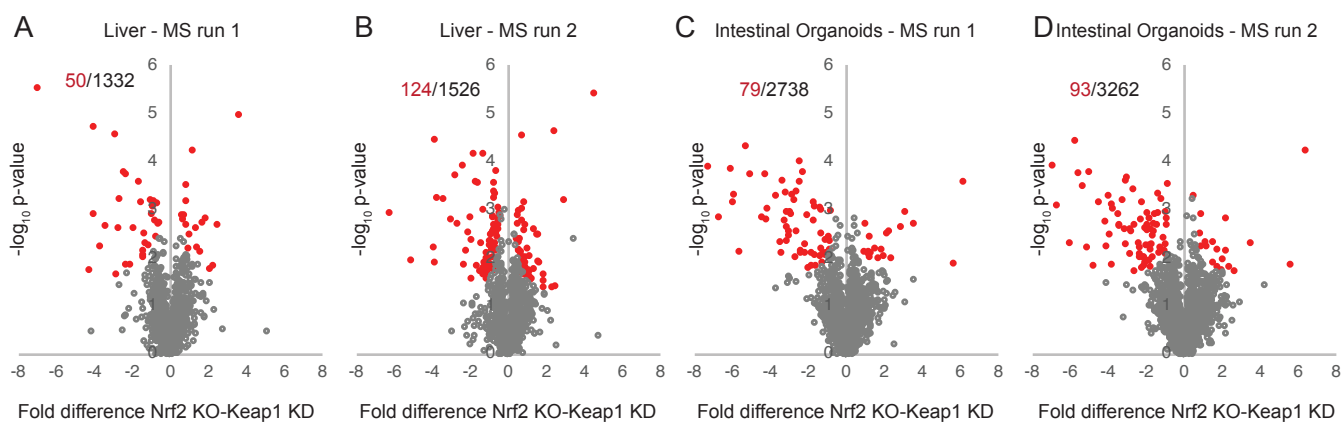
A Liver - MS run 1

50/1332

-log₁₀ p-value

Fold difference Nrf2 KO-Keap1 KD

B Liver - MS run 2

124/1526

-log₁₀ p-value

Fold difference Nrf2 KO-Keap1 KD

C Intestinal Organoids - MS run 1

79/2738

-log₁₀ p-value

Fold difference Nrf2 KO-Keap1 KD

D Intestinal Organoids - MS run 2

93/3262

-log₁₀ p-value

Fold difference Nrf2 KO-Keap1 KD

Figure S1. Proteomic analyses of mitochondria-enriched preparations from liver and early-passage intestinal organoids from wild-type (WT), Nrf2-knockout (Nrf2-KO), and Keap1-knockdown (Keap1-KD) mice. Fold change versus t-test p-value results for proteins quantified in each MS run for liver (A,B) and intestinal organoids (C,D). Red markers are those proteins that met the statistical cutoff of 10% FDR and S0=0.1 in two samples unpaired Student's t-test. See Data S1 for details. Related to Figure 1.

Liver

STRING protein interaction networks

A   **Protein processing in endoplasmic reticulum and signal peptidase complex**
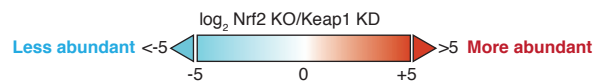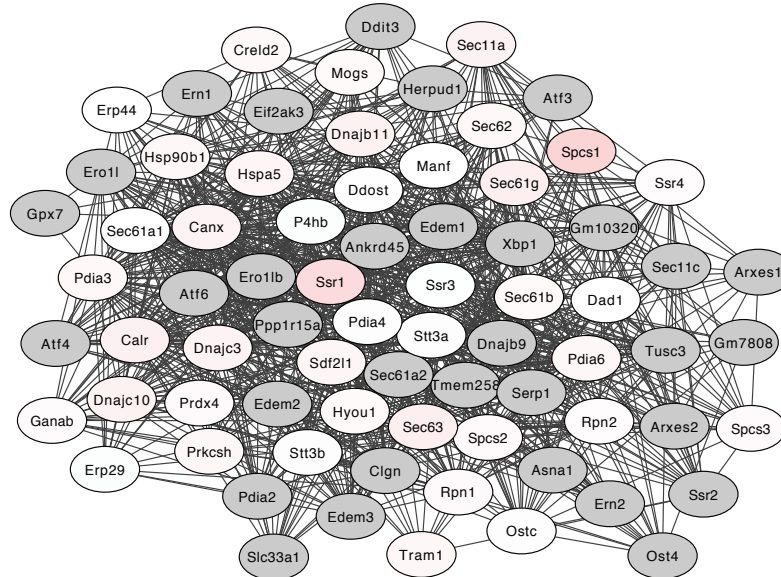
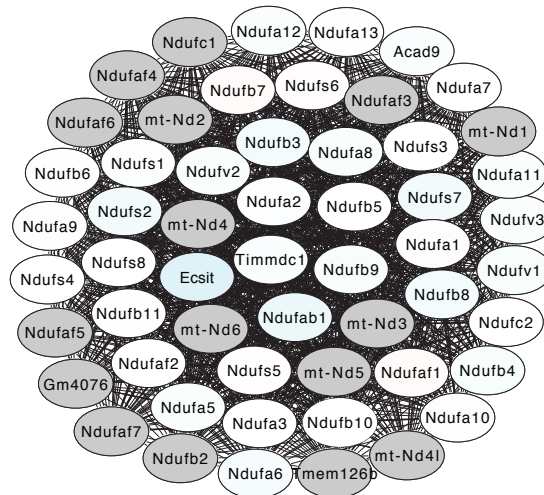**B**   **Mitochondrial Complex I biogenesis**

Figure S2. Network of proteins identified by STRING with both functional enrichments and quantitative relationships in mitochondria-enriched preparations from livers of Nrf2-knockout (Nrf2-KO) and Keap1-knockdown (Keap1-KD) mice. In addition to clusters of metabolic proteins within the Ces1 and Ugt families shown in Figure 2A, this type of analysis identified proteins with roles in protein processing in endoplasmic reticulum and signal peptidase complex (A), and proteins involved in mitochondrial complex I biogenesis (B) as statistically significantly different between the Nrf2-KO and Keap1-KD genotypes. Related to Figure 2.

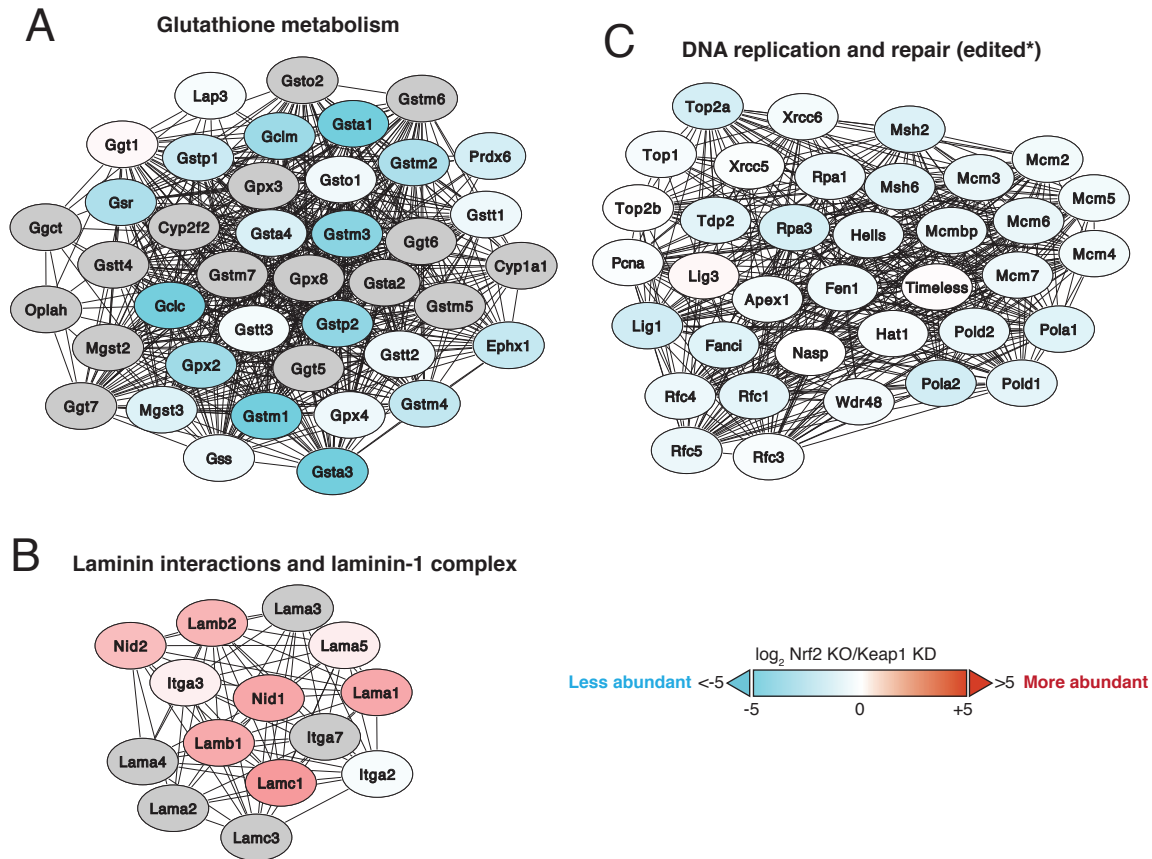# Intestinal organoids STRING protein interaction networks

A   Glutathione metabolism

B   Laminin interactions and laminin-1 complex

C   DNA replication and repair (edited*)

log$_2$ Nrf2 KO/Keap1 KD

Less abundant <-5   >5 More abundant

-5   0   +5

Figure S3. Network of proteins identified by STRING with both functional enrichments and quantitative relation-ships in mitochondria-enriched preparations from early-passage intestinal organoids from Nrf2-knockout (Nrf2-KO) and Keap1-knockdown (Keap1-KD) mice. In addition to clusters of metabolic proteins within the Ces1 and Cyp families shown in Figure 2B, and proteins involved in glycolysis and the pentose phosphate pathway shown in Figure 3A, this type of analysis identified glutathione metabolism (A), extracellular matrix proteins (B), and a group of DNA replication and repair proteins (C) as statistically significantly different between the Nrf2-KO and Keap1-KD genotypes. Related to Figures 2 and 3.
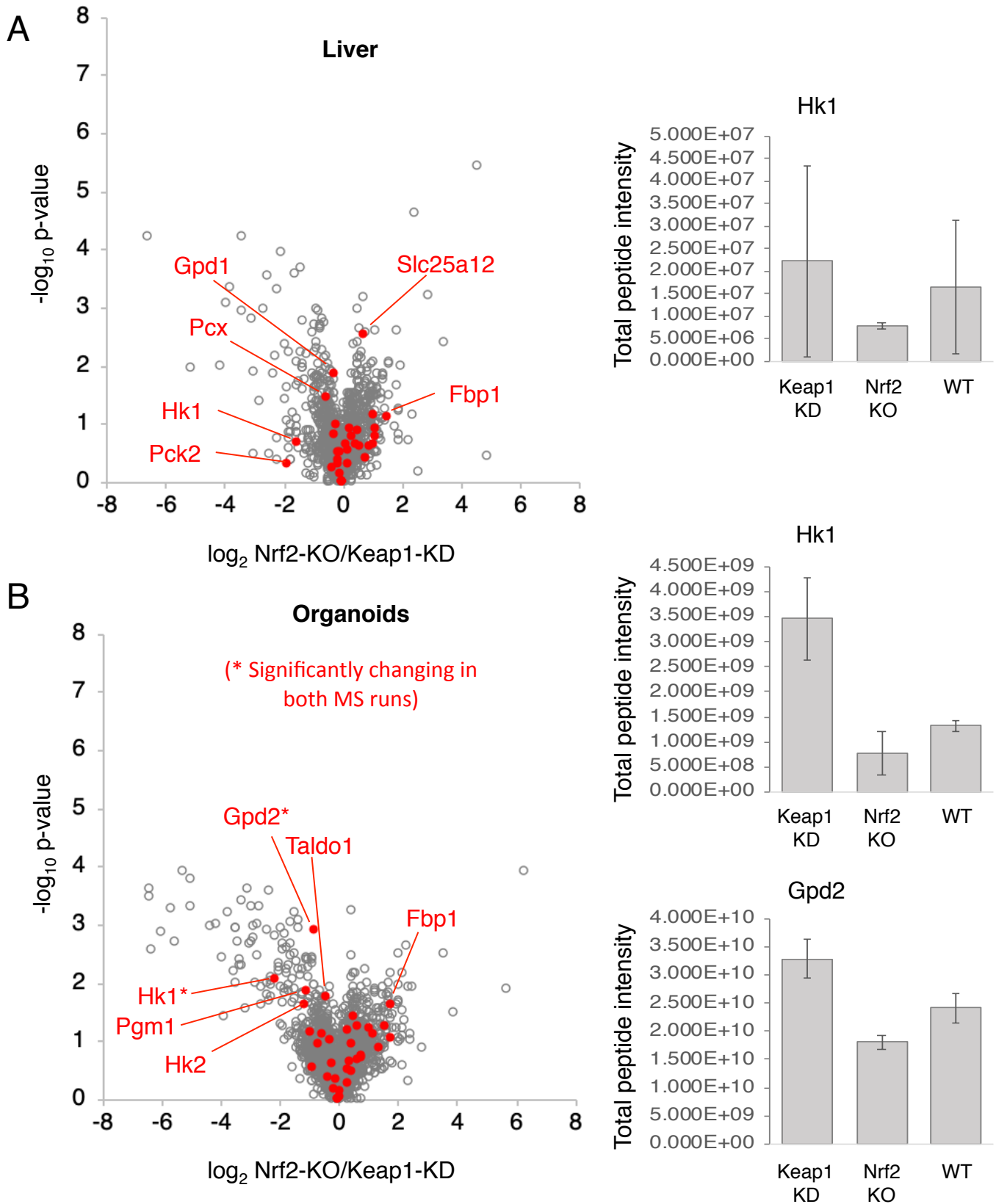
Figure S4. Proteomic analyses of enzymes related to gluconeogenesis in mitochondria-enriched preparations from liver and early-passage intestinal organoids from wild-type (WT), Nrf2-knockout (Nrf2-KO), and Keap1-knockdown (Keap1-KD) mice. Fold change versus t-test p-value results for proteins quantified in the two MS runs for liver (A) and intestinal organoids (B). Red markers are proteins related to gluconeogenesis. Those that met the statistical cutoff of 10% FDR and S0=0.1 in two samples unpaired Student's t-test are indicated with an asterisks. The side panels show the protein intensities for Hk1 (liver), and for Hk1 and Gpd2 (organoids) in the three genotypes. Related to Figure 3.
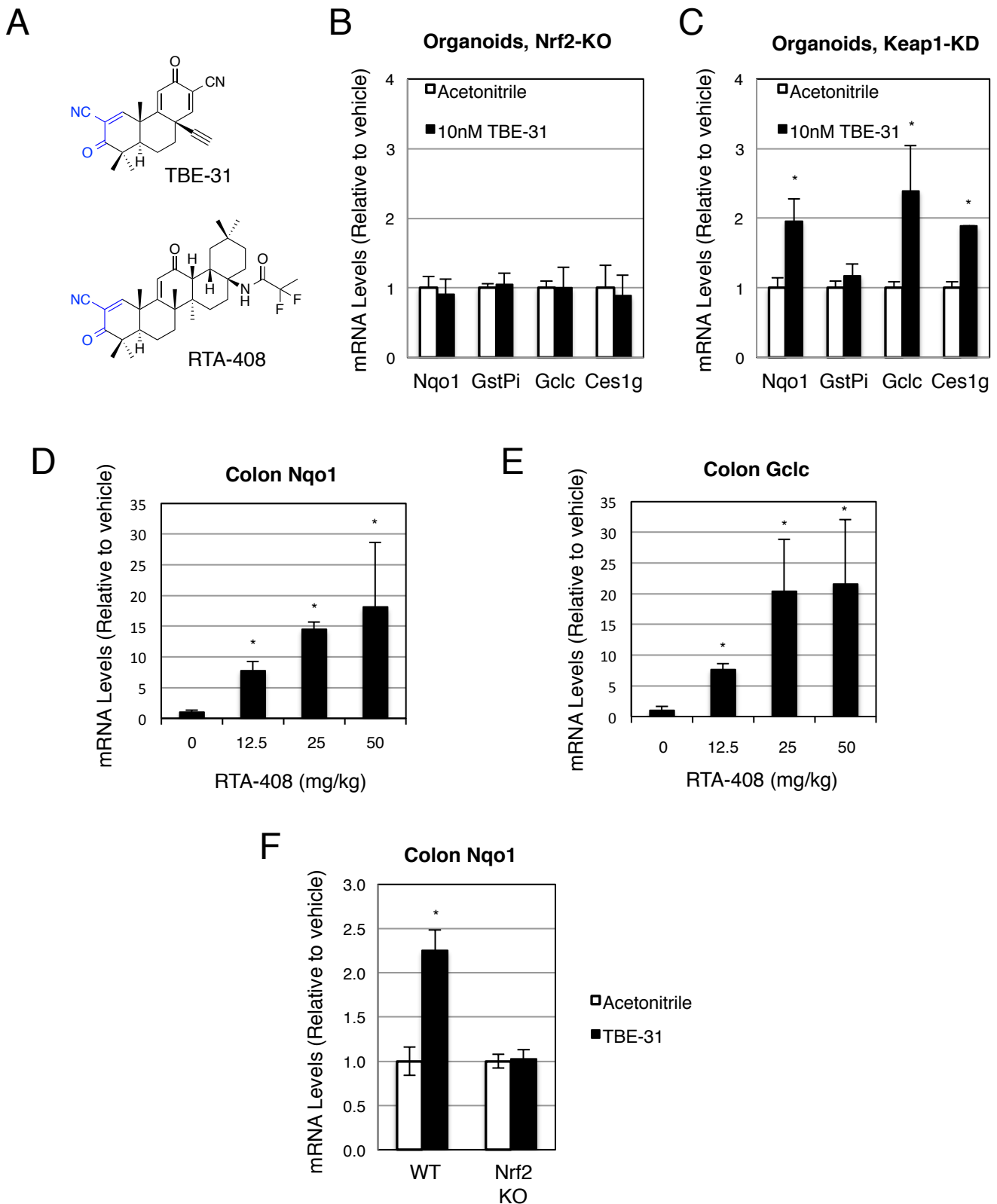
Figure S5. The cyclic cyanoenones TBE-31 and RTA-408 activate Nrf2-dependent transcription. (A) Chemical structures of TBE-31 and RTA-408. (B,C) mRNA levels for Nqo1, Gstp, Gclc and Ces1g in intestinal organoids from Nrf2-knockout (Nrf2-KO) (B) and Keap1-knockdown (Keap1-KD) (C) mice. The organoids (n=3) were treated with the Nrf2 activator TBE-31 (10 nM, 16h) or vehicle (0.1% acetonitrile). (D,E) mRNA levels for Nqo1 (D) and Gclc (E) in colons of male WT C57BL6 mice (n=3-4) that had been treated with RTA-408, *per os*, 3 times, 24h-apart, and colon tissue was harvested 6h after the last dose. (F) mRNA levels for Nqo1 in colons of male C57BL6 wild type (WT) and Nrf2-knockout (Nrf2-KO) mice (n=4-5). The animals were treated with TBE-31 (5 nmol/g body weight, 3 times, at 24-h intervals, *per os,* black bars) or vehicle (1% DMSO in corn oil, white bars), and fasted for 4h before tissue harvesting. Related to Figure 4.
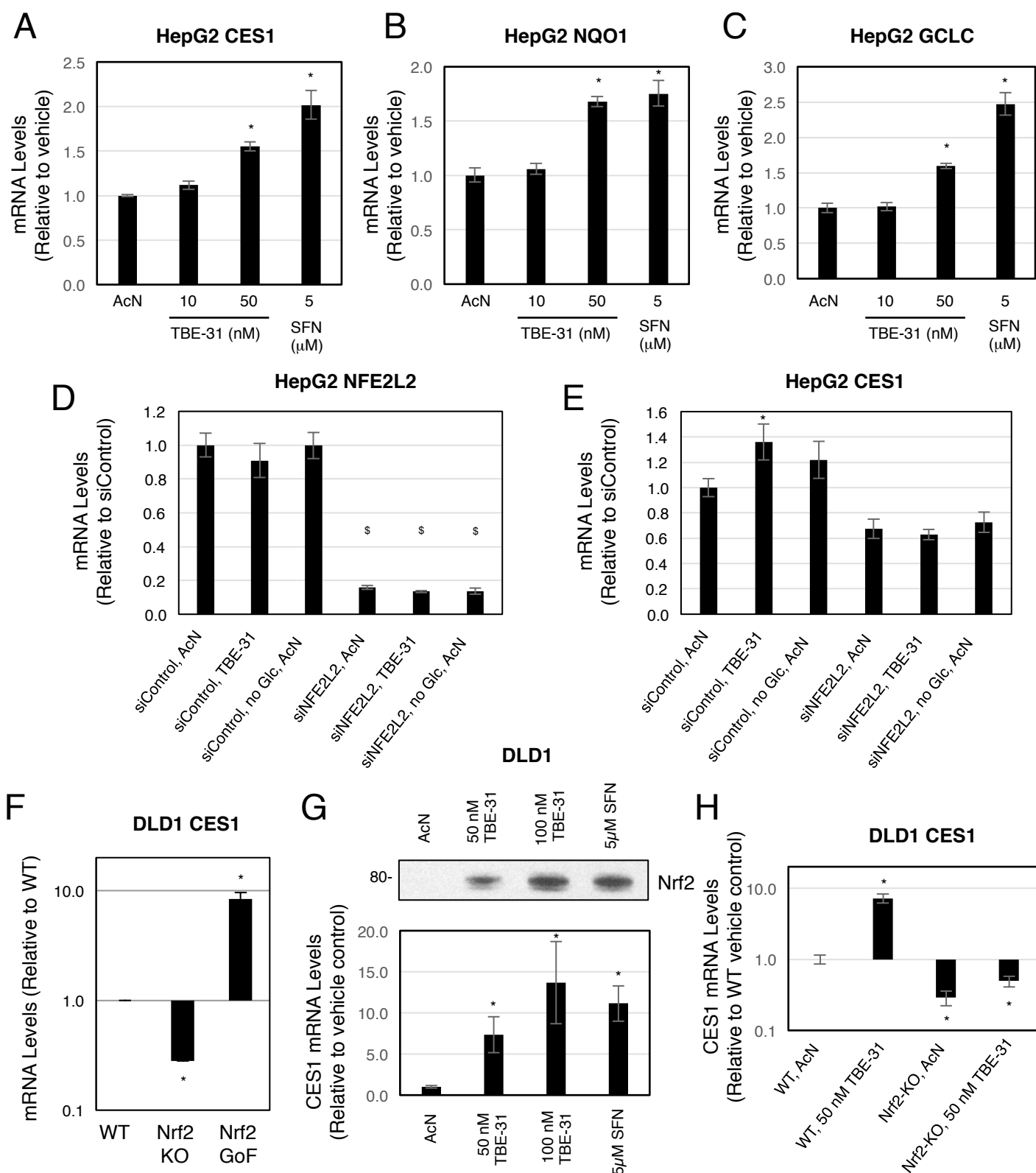
Figure S6. Nrf2 dependence of human CES1 expression. (A-C) mRNA levels for CES1 (A), NQO1 (B) and GCLC (C) in HepG2 cells following 16h treatment with Nrf2 activators TBE-31 (10 and 50 nM), SFN (5 μM) or vehicle (0.1% acetonitrile). (D-E) mRNA levels for *NFE2L2* (D) and CES1 (E) in HepG2 cells following siRNA knock-down of *NFE2L2* for 45h combined with TBE-31 (100nM, last 16h) or glucose deprivation (last 27h), or vehicle control treatment (0.1% acetonitrile). (F) mRNA levels for CES1 in isogenic DLD1 cell lines with either unaltered Nrf2 (WT), or Nrf2-knockout (Nrf2-KO) or Nrf2-gain-of-function (Nrf2-GoF) mutations. (G) Nrf2 protein (top panel) and CES1 mRNA levels (bottom panel) in DLD1 cells following 17h treatment with Nrf2 activators TBE-31 (50 and 100 nM), SFN (5 μM) or vehicle (0.1% acetonitrile). (H) CES1 mRNA levels in unaltered (WT) and Nrf2-knockout (Nrf2-KO) isogenic DLD1 cell lines following 17h treatment with Nrf2 activator TBE-31 (50 nM) or vehicle (0.1% acetonitrile). *p<0.01, relative to the respective leftmost control (A,B,C,E,G,H,F); $p<0.01, changes in response to si*NFE2L2* treatment (D). Related to Figure 4.
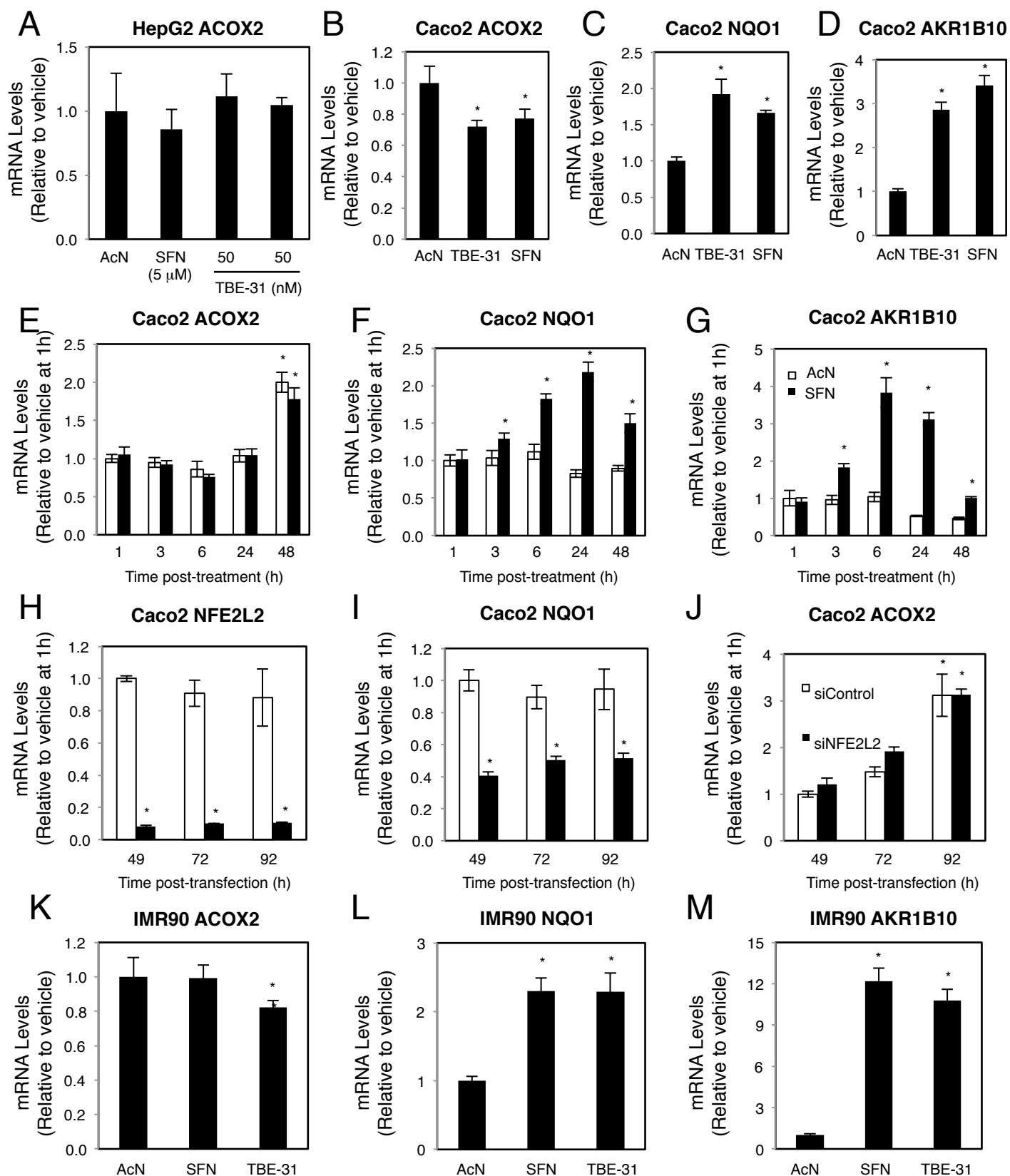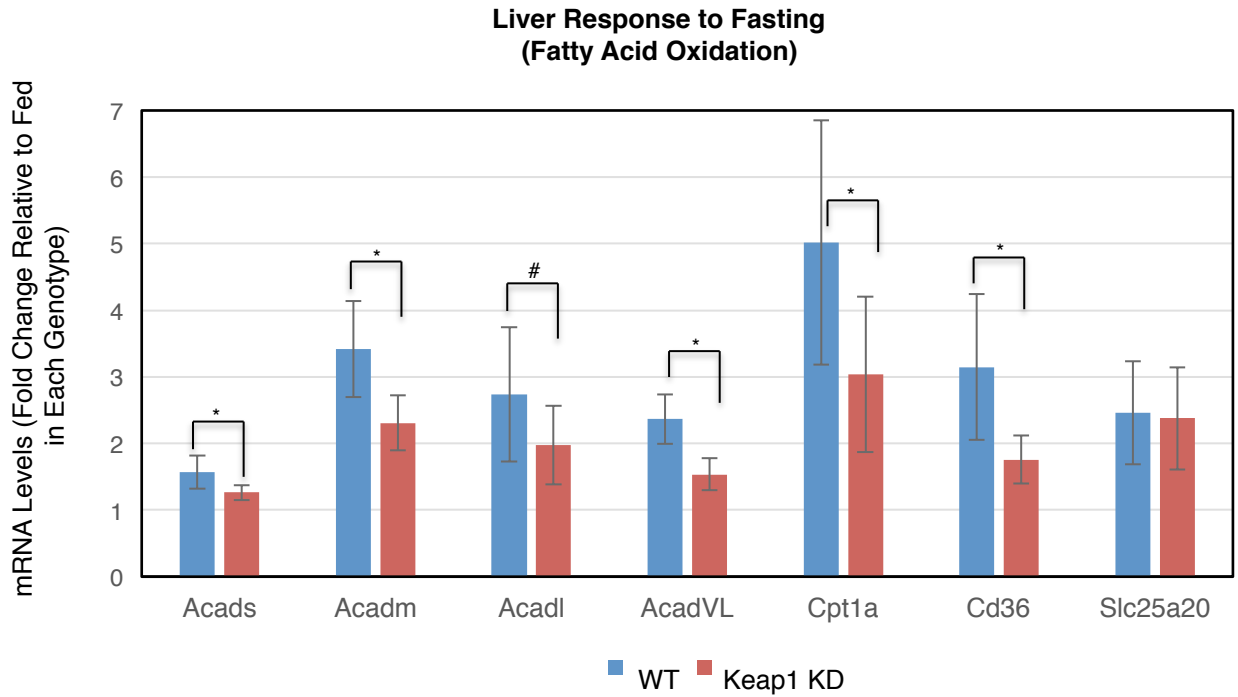
Figure S7. (A) mRNA levels for ACOX2 in HepG2 cells following 16h treatment with Nrf2 activators SFN, TBE-31, or vehicle (0.1% acetonitrile). (B-D) mRNA levels for ACOX2 (B), NQO1 (C) and AKR1B10 (D) in Caco2 cells following 16h treatment with Nrf2 activators TBE-31 (100 nM), SFN (5 μM) or vehicle in serum-free media. (E-G) mRNA levels for ACOX2 (E), NQO1 (F) and AKR1B10 (F) in Caco2 treated with the Nrf2 activator SFN (5 μM, black bars) or vehicle (white bars) for the indicated times. *$p<0.05$, compared to vehicle at the 1h-time point. (H-J) mRNA levels for *NFE2L2* (H), NQO1 (I) and ACOX2 (J) in Caco2 following transfection with siRNA targeting *NFE2L2* (black bars) or no-targeting si-control (white bars) for the indicated times. *$p<0.05$, compared to vehicle at the 49h-time point. (K-M) mRNA levels for ACOX2 (K), NQO1 (L) and AKR1B10 (M) in IMR90 cells following 16h treatment with Nrf2 activators SFN (5 μM), TBE-31 (100 nM), or vehicle. *$p<0.05$, compared to vehicle. Related to Figure 4.

Figure S8. Fasting decreases the expression of hepatic Acly, Acss2 and the levels of acetyl-CoA. (A,B) mRNA levels for Acly in livers (A) and colons (B) from *ad libitum*-fed wild-type (WT) and Keap1-knockdown (Keap1-KD) female Skh1-hairelss mice (n=6); *18S* used as a reference gene. (C) Acetyl-CoA levels in livers from *ad libitum*-fed wild-type (WT) and Keap1-knockdown (Keap1-KD) female Skh1-hairelss mice (n=5-10); *p < 0.05. (D) mRNA levels for Acss2 in livers from wild-type (WT) and Keap1-knockdown (Keap1-KD) female C57BL/6 mice (n=8) that were either fed *ad libitum* or fasted for 18h; *18S* used as a reference gene; $p<0.01 and $$p<0.05, compared to respective fed genotype. (E) Protein levels for Acly in livers of fasted wild-type (WT) and Keap 1-knockdown (Keap1-KD) female Skh1-hairless mice (n=6). (F) Levels of AcK40-α-tubulin and α-tubulin in livers of fed (top blot) or overnight-fasted (bottom blot) wild-type (WT) and Keap1-knockdown (Keap1-KD) Skh1-hairless mice (n=5-6). Related to Figures 6 and 7.

A

**Liver Response to Fasting
(Fatty Acid Oxidation)**

B

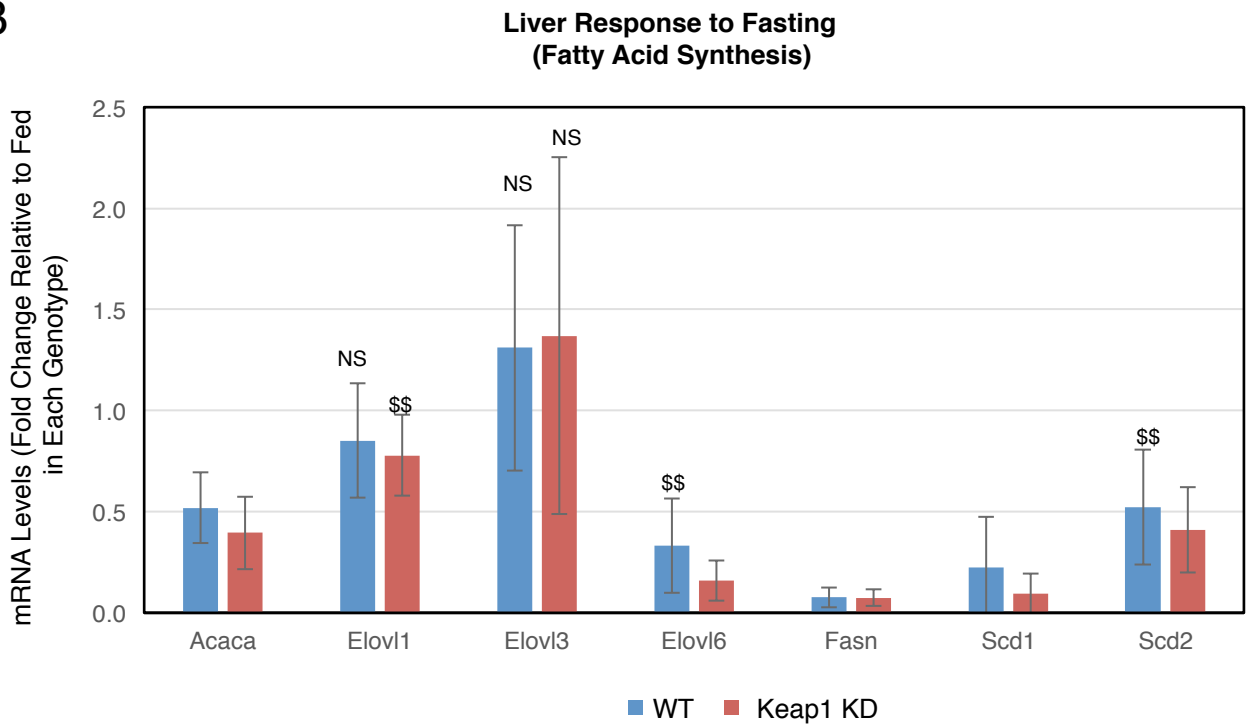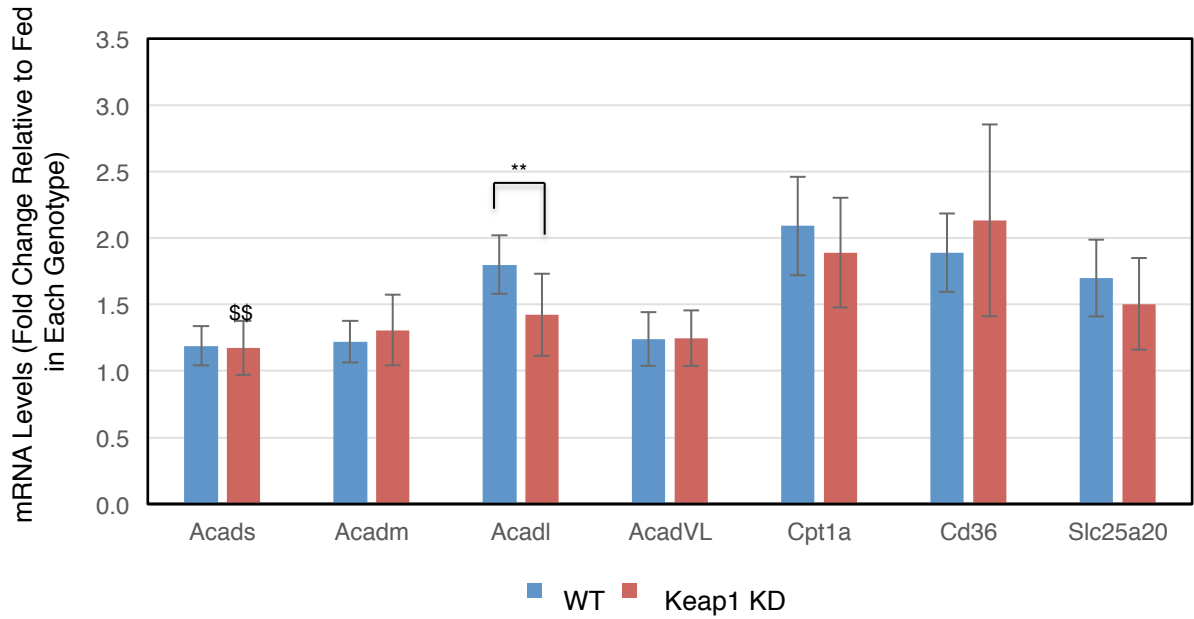**Liver Response to Fasting
(Fatty Acid Synthesis)**

Figure S9. Liver response to fasting. Fasted-to-fed ratios of mRNA levels for proteins involved in FAO (A) and FAS (B) in livers from wild-type (WT) and Keap1-knockdown (Keap1-KD) female C57BL/6 mice (n=8) that were either fed *ad libitum* or fasted for 18h. *18S* used as a reference gene. Effect of fasting on gene expression was significant ($p<0.01$, not shown) for all FAO genes (A) and most FAS genes (B) except where marked: $^{\$\$}0.01<p<0.05$, ^{NS} – non-significant; significance of the genotype and feeding status interaction (Type I Anova): $^*p<0.01$, $^\#0.05<p<0.1$. Related to Figure 6.

A Colon Response to Fasting
(Fatty Acid Oxidation)

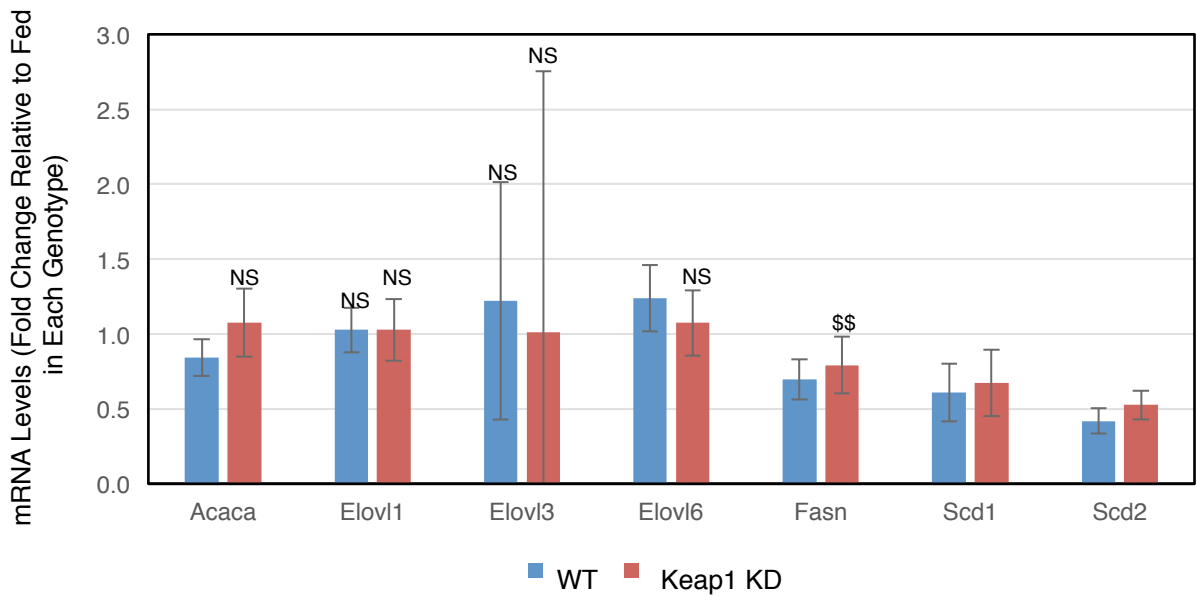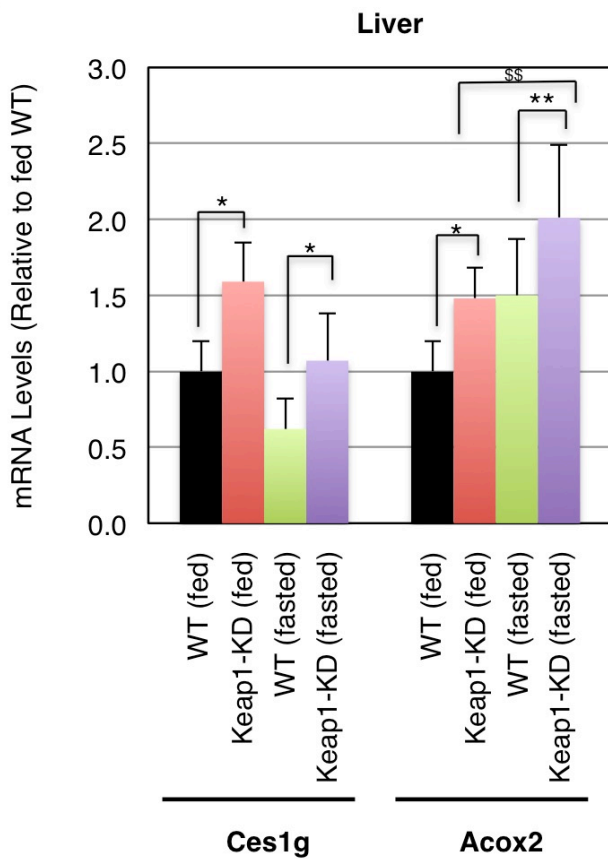**B** Colon Response to Fasting
(Fatty Acid Synthesis)

Figure S10. Colon response to fasting. Fasted-to-fed ratios of mRNA levels for proteins involved in FAO (A) and FAS (B) in colons from wild-type (WT) and Keap1-knockdown (Keap1-KD) female C57BL/6 mice (n=8) that were either fed *ad libitum* or fasted for 18h. *18S* used as a reference gene. Effect of fasting on gene expression was significant ($p<0.01$, not shown) for most FAO genes (A) and FAS genes (B) except where marked: $^{\$\$}$ $0.01<p<0.05$, ^{NS} – non-significant; significance of the genotype and feeding status interaction (Type I Anova): $^{**}0.01<p<0.05$. Related to Figure 6.
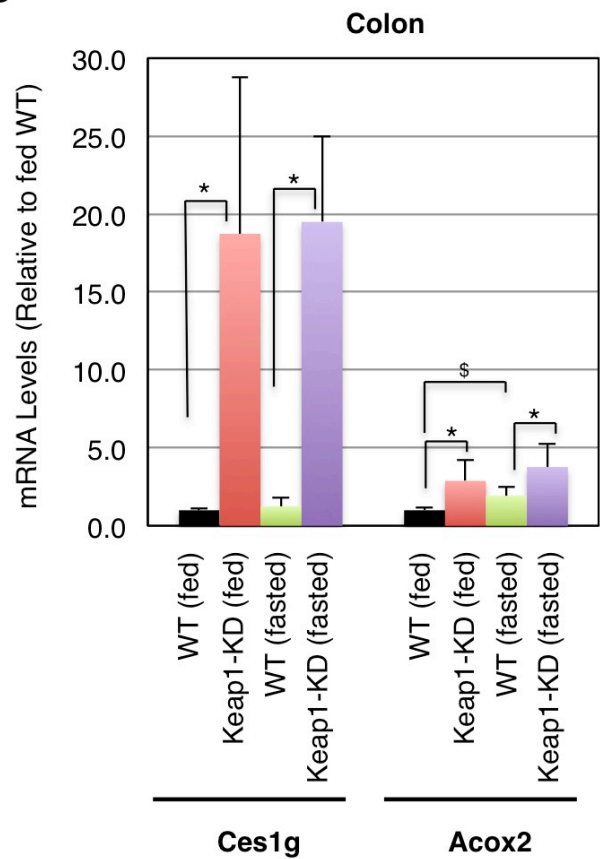
Figure S11. Downregulation of Keap1 increases the expression of Ces1g and Acox2 at fed and fasted states. mRNA levels for Ces1g and Acox2 in livers (A) and colons (B) from wild-type (WT) and Keap1-knockdown (Keap1-KD) female C57BL/6 mice (n=8) that were either fed *ad libitum* or fasted for 18h. *18S* used as a reference gene. Significance of the difference between the genotypes at the same feeding status: *$p < 0.01$, **$0.01 < p < 0.05$. Effect of fasting within each genotype in liver (A) was significant in all cases ($p < 0.01$, not labelled, $$$0.01 < p < 0.05$). Effect of fasting within each genotype in colon (B) did not reach significance except for Acox2 in WT ($$p < 0.01$). Related to Figures 4 and 6.
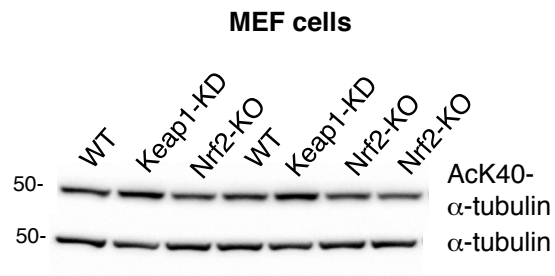
MEF cells

Figure S12. Downregulation of Keap1 increases, whereas depletion of Nrf2 decreases the acetylation of α-tubulin in mouse embryonic fibroblast (MEF) cells. Levels of AcK40-α-tubulin and α-tubulin in primary MEF cells from wild-type (WT), Nrf2-knockout (Nrf2-KO), and Keap1-knockdown (Keap1-KD) mice. Related to Figures 6 and 7.

TRANSPARENT METHODS

Materials

All chemicals and reagents were of the highest purity available and were purchased from common commercial suppliers. RTA-408 was from Cayman Chemical. *R,S*-sulforaphane (SFN) was from LKT Labs. (±)-TBE-31 was synthesized as described previously (Honda et al., 2011). For organoid culture experiments, a stock solution of TBE-31 in acetonitrile (AcN) was prepared and diluted (1:1,000) in the culture medium to achieve the final concentrations indicated in the figure legends. The final concentration of the solvent in the culture medium was 0.1% (v/v). For administration to animals by oral gavage, stock solutions of TBE-31 and RTA-408 in DMSO were prepared and diluted (1:100) in corn oil to achieve the compound doses indicated in the figure legends. The control mice received equal volumes of 1% DMSO in corn oil.

Antibodies

Solutions of primary antibodies were prepared in 5% (v/v) non-fat milk or 3% (w/v) BSA (anti-AcK40-α-tubulin only) in PBST. The following antibodies were used: rabbit polyclonal anti-carboxylesterase 1 (Ces1), 1:1,000, Abcam; rabbit monoclonal anti-acetylated (AcK40)-α-tubulin, 1:1,000, CST; mouse monoclonal anti-α-tubulin, 1:1,000, CST; rabbit polyclonal anti-ATP-citrate lyase (Acly), 1:1,000, CST; rabbit polyclonal anti-GAPDH, 1:5,000, Sigma; mouse monoclonal anti-β-actin, 1:10,000, Sigma; rabbit monoclonal LC3B, 1:1000, CST.

Animals

All mouse experiments were performed after ethical approval, in accordance with the regulations described in the UK Animals (Scientific Procedures) Act 1986. Mice were bred and maintained at the Medical School Resource Unit of the University of Dundee, with free access to water and food (pelleted RM1 diet from SDS Ltd., Witham, Essex, UK), on a 12-h light/ 12-h dark cycle, 35% humidity. Wild-type, Nrf2-knockout (Nrf2$^{-/-}$, N0) and Keap1-knockdown (Keap1$^{flox/flox}$, KD) mice (Taguchi et al., 2010) were originally generously provided by Masayuki Yamamoto (Tohoku University, Japan), and the resulting mouse colonies were maintained on either

C57BL/6 or Skh-1 hairless genetic backgrounds. Both male and female mice were used.

Isolation of mitochondria-enriched fractions from liver

To obtain mitochondria-enriched preparations from liver for proteomic analysis, 3 individual 20-22-week-old female mice of each genotype, all on the Skh-1 hairless genetic background, were used. The animals were euthanized by cervical dislocation, followed by decapitation and the blood was drained for 20 sec. All subsequent steps were performed on ice using pre-chilled solutions and instruments. Large bore pipette tips were used (made by cutting 2-3 mm off the standard tip end). Excised fresh whole livers were rinsed in 100 ml of ice-cold PBS and then in 50 ml of ice-cold Mitochondrial Isolation Buffer (MIB, 250 mM sucrose, 1mM EGTA, 20 mM Tris-Cl pH 7.4), transferred into a fresh beaker with 15 ml MIB on ice, chopped with scissors and then homogenised using Dounce homogeniser for 5 min on ice. Homogenates were clarified by centrifugation at 400 x g for 6 min (Sorvall T21, SL50T), and the resultant supernatants were transferred into fresh tubes and subjected to centrifugation, first at 1,200 x g for 6 min, followed by 8,000 x g for 10 min. The resulting pellets were gently re-suspended in 25 ml MIB, transferred into fresh tubes and subjected to centrifugation at 8,000 x g for 12 min. The supernatants were discarded and pellets washed twice by gently swirling the tube walls with 25 ml of MIB. The pellets were then carefully re-suspended in 1 ml MIB, frozen in aliquots in liquid nitrogen, and stored at -80°C until further use. Small aliquots of fractions from all purification steps were taken and analysed by immunoblotting for Vdac1, Lamin A and Actin B as quality control.

Preparation of mitochondrial proteins for tryptic digest

Mitochondrial-enriched fractions were thawed on ice and diluted 1:1 with MIB containing 1x Protease Inhibitors Cocktail (Roche). LDS loading buffer (4x, Thermo) and Sample Reducing Agent (Thermo) were added at 1:4 and 1:10 ratios, respectively, and the samples were incubated at 95°C for 5 min and sonicated for 25 sec at 25% amplitude. The insoluble material was removed by centrifugation for 10 min at 16,000 x g, the supernatant was transferred to a fresh tube. The protein

concentration was determined by the BCA assay (Thermo), and adjusted to the same protein concentration in all samples with MIB containing LDS and sample reducing agent. Proteins (24 µg) per lane were resolved on 10% Novex Bis-Tris NuPAGE gel, which was then fixed for 30 min in 50% v/v MeOH, 40% v/v Acetic acid, stained with Coomassie R stain (0.25% w/v Coomassie R, 50% v/v MeOH, 40% v/v Acetic acid) for 20 min, and de-stained for 3 hours with 3-4 changes of the de-staining solution (5% v/v MeOH, 7.5% v/v Acetic acid), and then in deionised water for 2 hours, with gentle agitation at room temperature.

Organoids

Organoids were generated from isolated intestinal crypts as described (Carroll et al., 2017; Sato et al., 2009). Mice were euthanized, small intestine was collected, and flushed with ice-cold PBS. The small intestine was cut open, and the villi were removed with a coverslip. After washing with ice-cold PBS, the intestine was incubated with 3 mM EDTA in PBS for 20 min on a rocker in a cold room. Crypts were obtained by mechanical shaking, followed by centrifugation at 4°C for 3 min at 76 x g and 3 washes with PBS to remove single cells and microorganisms. The pellet was washed with cold Advanced DMEM/F12 (ADF) and resuspended in 3 ml pre-warmed TrypLE Express at 37°C for 5 min to break crypts into individual cells. Once crypts were broken up, 7 ml ADF+100 µl of Pen/Strep was added. The suspension was passed through a 40-µm cell strainer (BD Biosciences) to filter out any large aggregates of cells. Single cells were then collected by centrifugation at 1349 x g for 3 min. The pellet was resuspended in a small volume of the remaining supernatant, mixed with phenol-free Matrigel (BD Biosciences) and seeded into a 24-well plate. The plate was placed into a 37°C incubator to solidify the Matrigel, following which 0.5 ml of crypt medium was added to each well. The crypt medium had the following composition: advanced DMEM/F12 supplemented with 10 mM HEPES, 20 mM Glutamax-1, N2 supplement, B27 supplement, penicillin-streptomycin, TrypLE Express (all from Invitrogen), N-acetylcysteine (Sigma), growth factors (EGF, 50 ng/ml, Invitrogen; Noggin, 100 ng/ml, Peprotech), and R-Spondin conditioned medium (1:4). During the first 48 h, 3 µM Chiron99021 and 1 mM valproic acid (both from Sigma) and 10 µM Y27632 (Cambridge Bioscience) were also added. The

resulting organoid cultures were passaged by washing with cold ADF medium followed by mechanical breaking of the Matrigel and organoids using a pipette. After a further wash, the organoids were mixed with 100 μl of fresh Matrigel and grown on 24-well plates in 5% CO_2 at 37°C. For gene expression analysis, RNA was extracted from organoids growing in 3 individual wells; these organoids originated from one animal of each genotype.

To obtain mitochondria-enriched preparations from organoids for proteomic analysis, cultured organoids from 3 individual 7-10 week-old animals of each genotype, all on the C57BL/6 genetic background, were used. The organoids were harvested with Corning™ Cell Recovery Solution (Fisher Scientific) following the manufacturer's instructions. Mitochondria-enriched fractions were prepared from WT, N0 and KD C57/BL6 mice (n=3) as described (Frezza et al., 2007). Briefly, organoid pellets were resuspended with ice-cold mitochondria isolation buffer (10 mM Tris/MOPS, 1 mM EGTA/Tris, 200 mM sucrose, pH 7.4) and homogenized with glass-Teflon potter homogenizer on ice. The homogenate was subjected to centrifugation at 600 × g for 10 min at 4°C to remove nuclei. The supernatant was then subjected to centrifugation at 7,000 × g for 20 min at 4°C to pellet the mitochondrial fraction. The pellet was washed once with ice-cold mitochondria isolation buffer, mitochondria were resupended in the same buffer, and protein concentrations were determined by the BCA assay (Thermo). The resuspended mitochondria-enriched fractions were mixed with NuPAGE LDS Sample Buffer (Thermo) and heated at 70°C for 10 min. NuPAGE™ Sample Reducing Agent (Thermo) was added into the samples, and proteins (14 μg) were resolved on 10% SDS-PAGE gel (with NuPAGE – MOPS buffer, Thermo).

Cells

Primary mouse embryonic fibroblast (MEF) cells were prepared from wild-type, Nrf2-knockout, and Keap1-knockdown Skh-1 hairless mice (Knatko et al., 2015). MEF cells were cultured in plastic dishes coated for 30 min with 0.1% (w/v) gelatin before use and grown in Iscove's modified Dulbecco's medium (with L-glutamine) (IMDM) supplemented with human recombinant EGF (10 ng/mL), 1 ×

insulin/transferring/selenium, and 10% (v/v) heat-inactivated fetal bovine serum (FBS, Thermo Scientific). Isogenic human colorectal cancer DLD1 cell lines with either Nrf2-knockout (Nrf2-KO) or Nrf2-gain-of-function (Nrf2-GoF) mutations and Nrf2-KO lung cancer A549 cells were generated using CRISPR/Cas9 genome editing as described (Torrente et al., 2017) and confirmed by sequencing. DLD1, A549 and human liver cancer HepG2 cells were grown in Dulbecco's Modified Eagle Medium (DMEM, Gibco, Thermo Scientific) that contains L-glutamine, sodium pyruvate, and high D-glucose content (4.5 g/L) supplemented with 10% (v/v) heat-inactivated FBS. The human colorectal cancer cell line Caco2 was cultured in DMEM supplemented with 10% (v/v) heat-inactivated FBS and 1% MEM Non-essential Amino Acid Solution (Sigma). The human normal lung fibroblast cell line IMR90 was grown in DMEM supplemented with 20% (v/v) heat-inactivated FBS and 2mM L-Glutamine (Gibco, Thermo Scientific). All cell cultures were maintained in 5% CO_2 at 37°C and were routinely tested to ensure that they were mycoplasma-free.

Small interfering RNA (siRNA) transfection

Caco2 and HepG2 cells were transfected with 20 nM ON-TARGET plus Smart Pool siRNA against human *NFE2L2* (L-003755-00-0005, Horizon Discovery) or ON-TARGET plus Non-targeting Control Pool (D-001810-10-50, Horizon Discovery) using Lipofectamine® RNAiMAX (Thermo Scientific) following manufacture's instruction. In brief, siRNA targeting *NFE2L2*/non-targeting control and Lipofectamine® RNAiMAX were mixed in Opti-MEM (Gibco, Thermo Scientific) and incubated for 20 min at room temperature. At the same time, cells were trypsinized as normal and diluted to 1 x 10^5 cells per ml of medium. 500 µl of the RNAiMAX/siRNA/Opti-MEM was aliquoted into each well of a 6-well plate, to which 2 ml of the diluted cell suspension was added, and gently mixed. Cells were harvested at 2,3 and 4 days after transfection for further analysis.

Real-time quantitative PCR

Total RNA was extracted from cultured cells, organoids and mouse liver and colon using RNeasy Kit (Qiagen Ltd.). Omniscript RT Kit (Qiagen Ltd.) was then used to reverse-transcribe 500 ng of total RNA into cDNA. Real-time PCR was carried out on

Applied Biosystems QuantStudio™ 5 Real-Time PCR System. The TaqMan data for the mRNA species were normalized using mouse ribosomal protein lateral stalk subunit P0 (Rplp0), actin-beta, and 18S rRNA as internal controls. For human samples, human hypoxanthine phosphoribosyltransferase 1 (Hprt1) was used as an internal control. The TaqMan™ Gene Expression Assay IDs (Thermo) used are listed below.

Gene Name	Assay ID
18S	Hs99999901_s1
Acaca (mouse)	Mm01304257_m1
Acadl (mouse)	Mm00599660_m1
Acadm (mouse)	Mm01323360_g1
Acads (mouse)	Mm00431617_m1
Acadvl (mouse)	Mm00444293_m1
Acly (mouse)	Mm01302282_m1
Acox2 (mouse)	Mm00446408_m1
Acss2 (mouse)	Mm00480101_m1
Actb (mouse)	Mm00607939_s1
Cd36 (mouse)	Mm00432403_m1
Ces1f (mouse)	Mm00523518_m1
Ces1g (mouse)	Mm00491334_m1
Cpt1a (mouse)	Mm01231183_m1
Elovl1 (mouse)	Mm01188316_g1
Elovl3 (mouse)	Mm00468164_m1
Elovl6 (mouse)	Mm00851223_s1
Fasn (mouse)	Mm00662319_m1
Gclc (mouse)	Mm00802655_m1
Gstp1 (mouse)	Mm04213618_gH
Nqo1 (mouse)	Mm01253561_m1
Rplp0 (mouse)	Mm00725448_s1
Scd1 (mouse)	Mm00772290_m1
Scd2 (mouse)	Mm01208542_m1
Slc25a20 (mouse)	Mm00451571_m1
ACOX2 (human)	Hs00185873_m1
AKR1B10 (human)	Hs00252524_m1
CES1 (human)	Hs00275607_m1
GCLC (human)	Hs00155249_m1
HPRT1 (human)	Hs02800695_m1
NFE2L2 (human)	Hs00975961_g1
NQO1 (human)	Hs00168547_m1

Immunoblotting

Frozen tissues (liver and colon) were pulverised under liquid nitrogen using a mortar and pestle. Colon tissue powder (15 mg) was homogenized in 10 volumes of ice-cold RIPA buffer (50 mM Tris-HCl, pH 7.5, 150 mM NaCl, 1% NP-40, 0.1% SDS, 1% sodium

deoxycholate), supplemented with EDTA-free protease inhibitors cocktail (Roche) on a rotator wheel for 1 hour at 4°C. Liver tissue powder (15 mg) was homogenized for 20 sec in 10 volumes of ice-cold assay buffer from the PicoProbe acetyl-CoA assay kit (Abcam, ab87546) supplemented with EDTA-free protease inhibitors cocktail (Roche) using rotor-stator homogeniser (Physcotron NS310-E3, Microtech, Japan). The insoluble material was removed by centrifugation for 10 min at 16,000 x g at 4°C. An aliquot of the supernatant was taken for determination of protein concentration by the bicinchoninic acid (BCA) assay (Thermo). To the remaining supernatant, 4 x LDS loading buffer (Thermo) was added to achieve a final 1 x concentration, and the protein concentration was adjusted using LDS in RIPA buffer to the same protein concentration in all samples. Sample Reducing Agent (Thermo) was added, and the samples were incubated at 70°C for 10 min prior to electrophoresis.

Cells were washed once with PBS before lysing in SDS Laemmli loading buffer (62.5 mM Tris-HCl, pH 6.8, 2% SDS, 10% glycerol, 0.02% Bromophenol Blue); the volume of lysis buffer was between 100-150 μl depending on the cell confluence. Lysates were then transferred into Eppendorf tubes, boiled for 5 min, sonicated for 20 sec at 20% amplitude using Vibra-Cell ultrasonic processor (Sonic). Protein concentrations were determined by the bicinchoninic acid (BCA) assay (Thermo). A solution of bromophenol blue (5%, v/v) was then added to each sample, and the volume was adjusted to achieve the same protein concentration in all samples. Proteins were resolved by electrophoresis using pre-cast 4-12% gradient NuPage™ gels (Life Technologies) or hand-cast, 8% Tris-Glycine gels, and transferred onto nitrocellulose membranes (Amersham Biosciences). Membranes were blocked in either 5% non-fat milk or 3% BSA for 45 min, on a rocker (60-70 rpm), at room temperature, and then incubated with the primary antibodies at 4°C on a rocker overnight.

Determination of autophagic flux

Parental A549 or Nrf2-KO A549 cells were seeded at a density of 3 x 10^5 cells per well of a 6-well plate. After 20-24 h, cells were treated with either vehicle (0.1% DMSO) or 10 nM Bafilomycin A (BAF) for 16 h. Following the treatment, the cells were washed thrice with PBS and lysed in 150 μL of SDS lysis buffer [50 mM Tris-HCl pH

6.8, 2% SDS (w/v), 10% Glycerol (v/v) and 0.005% Bromophenol Blue (w/v)]. The lysates were subjected to sonication for 20 sec at 20 % amplitude. Protein concentrations were determined using the BCA assay (Thermo), and equal amounts of protein (10-20 µg) from each sample was loaded into each well of a 15% Tris-Glycine SDS polyacrylamide gel and subjected to electrophoresis. Once the proteins were resolved on the gel, they were transferred onto 0.45-µm premium nitrocellulose membranes (Amersham Biosciences) using wet electroblotting transfer system (Bio-Rad). Subsequently, the membranes were blocked in PBST-milk [5% (w/v) non-fat milk dissolved in PBS-0.01 % Tween (v/v)] for 1 h at room temperature (RT). Following blocking, the membranes were incubated overnight at 4°C with either the LC3B or GAPDH antibody diluted in PBST-milk. Next, the membranes were washed thrice for 30 min with PBS-0.01% Tween and incubated with the respective fluorescently-labeled IRDye$^®$ secondary antibodies 1:20,000 (LI-COR) for 1 hour at room temperature, and were protected from light. After incubation with the secondary antibodies, the immunoblots were washed thrice for 30 min with PBS-0.01% Tween before scanning using the Odyssey CLx Near-Infrared Fluorescence Imaging System (LI-COR). The images obtained were analysed in the Image Studio software (Version 4.0.21).

Determination of triglycerides and acetyl-CoA
Triglycerides were determined using Trigyceride Assay Kit (Abcam, ab65336) according to the manufacturer's instructions for the colorimetric detection method. Briefly, frozen tissues were pulverised under liquid nitrogen followed by extraction in 5% NP-40 (10 µl per mg of tissue). Two µl of extract was used per assay well, in triplicates.

Acetyl-CoA was measured using PicoProbe Acetyl CoA Assay kit (Abcam, ab87546) according to the manufacturer's instructions for tissue samples. In brief, frozen tissues were pulverised under liquid nitrogen, homogenised in 1M ice-cold HClO$_4$ (2 µl per 1 mg tissue), the precipitants were removed by centrifugation for 10 min at 10,000 x g at 4°C, and the supernatants neutralized with 3M KHCO$_3$. 10 µl of clear supernatants were used per assay reaction.

Proteomics

For both proteomic experiments, proteins from mitochondrial preparations of three types, namely WT control (WT), Nrf2 knockout (Nrf2-KO), and Keap1 knockdown (Keap1-KD), were fractionated by SDS-PAGE and excised into two gel sections per lane. Peptides were extracted by tryptic digestion (Shevchenko et al., 2006), including alkylation with iodoacetamide. Peptide samples were analyzed by LC-MS/MS on a Q Exactive mass spectrometer (Thermo Scientific) coupled to an EASY-nLC 1000 liquid chromatography system via an EASY-Spray ion source (Thermo Scientific) running a 75 μ m x 500 mm EASY-Spray column at 45°C. Data were acquired in the data-dependent mode. Full scan spectra (m/z 300–1800) were acquired with resolution R = 70,000 at m/z 200 (after accumulation to a target value of 1,000,000 with maximum injection time of 20 ms). The 10 most intense ions were fragmented by HCD and measured with a resolution of R = 17,500 at m/z 200 (target value of 500,000, maximum injection time of 60 ms) and intensity threshold of 2.1×10^{4}. Peptide match was set to 'preferred' and a 40 second dynamic exclusion list was applied. For each experiment two elution gradients were used: Liver – 60 min and 240 min, Intestinal organoids – 140 min and 180 min.

Raw MS data files were processed using MaxQuant (v 1.6.1.0) with the built-in Andromeda peptide search engine (version 1.3.0.5) (Cox and Mann, 2008; Cox et al., 2011). The mouse uniprot protome was searched (downloaded October 2019 – 55153 entries). Enzyme specificity was set to trypsin-P. Cysteine carbamidomethylation was selected as a fixed modification with methionine oxidation and protein N-terminal acetylation as variable modifications. Initial maximum allowed mass deviation was set to 20 parts per million (ppm) for peptide masses and 0.5 Da for MS/MS peaks. The minimum peptide length was set to 7 amino acids and maximum size 4600 Da. A maximum of two missed cleavages were considered. A false discovery rate (FDR) of 1% was required at both the protein and peptide levels. Label-free quantification was selected and the 'match between runs' option was applied with a time window of two minutes.

The unfiltered proteinGroups.txt file (**Data S1**, Quantitative proteomics data) contained 6259 protein group entries, which after filtering for decoy proteins, those identified only by modified peptide(s), putative contaminants and those without a complete set of three LFQ values in at least one set of triplicates in at least one MS run, left 3752 proteins. Prior to further statistical analysis, LFQ values were further manually normalized within each MS run by median ratio of lane protein intensity/average of all lanes protein intensity for all common proteins for each slice (upper or lower). Once normalized, a single normalized LFQ value for each replicate in each MS run was calculated by the sum of the two slices normalized LFQ intensity for each peptide. This was necessary as output LFQ values were apparently not appropriately normalized when replicates were compared. Statistical analyses were performed using Perseus (v 1.6.1.1) (Tyanova et al., 2016). Data were separated into the four MS runs (two for liver and two for organoids samples). Zero values were replaced using Perseus default settings, and comparisons among cell types was performed using a two-tailed Student's t-test with cutoffs set at 10% FDR with an S0 value of 0.1. Data for all four MS runs were recombined into a single Excel file (**Data S1**, Quantitative proteomics data; "Accepted" sheet). The mass spectrometry proteomics data have been deposited to the ProteomeXchange Consortium via the PRIDE (Perez-Riverol et al., 2019) partner repository with the dataset identifier PXD021639.

STRING functional enrichment analyses were performed as follows. For both liver (1590 entries) and intestinal organoid (3335 entries) experiments, gene sets and quantitative data were uploaded to STRING (December 2019) using the 'Proteins with values/ranks" tool (Szklarczyk et al., 2019). This looks for functional enrichments among proteins deviating away from log_2 ratio=0, and therefore cellular functions potentially regulated by the experimental conditions (see **Data S2**, STRING functional group enrichment analysis for a full list of enrichments). Networks of proteins with high enrichment scores (extreme ratios), and low FDR values (high statistical significance) were selected for presentation.

Metabolomics

Metabolites were extracted using the methanol/chloroform/water (2:2:1; v/v) method described previously (Wang et al., 2015; West et al., 2016). Briefly, 50 mg of wet weight tissue was mixed with 600 µl of $CH_3OH/CHCl_3$ (2:1; v/v), and the samples were homogenized with a Tissuelyser (Qiagen, UK) for 5 min at a frequency of 20/s and sonicated for 15 min. Water and chloroform (each of 200 µl) were added to the samples before centrifugation at 13,300 rpm for 20 min. The resulting aqueous and organic phases were separated from the protein pellets. The extraction procedure was repeated on the remaining protein pellets. Both organic and aqueous phases were collected and evaporated to dryness. The dried samples were stored at −80°C until further analysis.

FAME Analysis

50 µl of D-25 tridecanoic acid (200 µM in chloroform), 650 µl of chloroform/methanol (1:1 v/v) and 125 µl BF_3/methanol (Sigma-Aldrich) was added to 100 µl organic extract dissolved in chloroform/methanol (1:1 v/v) (a quarter of the organic material extracted for each sample). The samples were then incubated at 80 ºC for 90 min. 500 µl H_2O and 1 ml hexane were added and each vial mixed. The organic layer was evaporated to dryness before reconstitution in 200 µl hexane for analysis. Using a Trace GC Ultra coupled to a Trace DSQ II mass spectrometer (Thermo Scientific, Hemel Hempstead, UK), 4 µl of the derivatised organic metabolites were injected onto a TR-fatty acid methyl ester (FAME) stationary phase column (Thermo Electron; 30 m × 0.25 mm ID × 0.25 µm; 70% cyanopropyl polysilphenylene-siloxane) with a split ratio of 20. The injector temperature was 230°C and the helium carrier gas flow rate was 1.2 ml/min. The column temperature was 60°C for 2 min, increased by 15°C/min to 150°C, and then increased at a rate of 4°C/min to 230°C (transfer line = 240°C; ion source = 250°C, EI = 70 eV). The detector was turned on after 240 s, and full-scan spectra were collected using 3 scans/s over a range of 50–650 m/z. Peaks were assigned using the Food Industry FAME Mix (Restek 6098).

LC-MS analysis of aqueous metabolites

Half of the extracted aqueous samples were reconstituted in 7:3 acetonitrile: 0.1 M aqueous ammonium carbonate containing 2 μM [$^{13}C_{10}^{15}N_5$] adenosine monophosphate, [$^{13}C_{10}^{15}N_5$] adenosine triphosphate, 10 μM [$^{13}C_4$] succinic acid and 10 μM [$^{13}C_5^{15}N_5$] glutamic acid (all from Sigma Aldrich except the glutamic acid from Cambridge Isotope Laboratories) as internal standards. The samples were vortexed then sonicated for 15 min followed by centrifugation at 21,000 x *g* to pellet any remaining undissolved material. They were analyzed on a Quantiva triple stage quadrupole mass spectrometer coupled to a Vanquish Horizon (all analytical instrument combinations supplied by Thermo Fisher Scientific), using a bridged ethylene hybrid (BEH) amide hydrophilic interaction liquid chromatography (HILIC) column, as previously described (Cader et al., 2020). The strong mobile phase (A) was 100 mM ammonium carbonate, the weak mobile phase was acetonitrile (B) with water:acetonitrile (1:1) being used for the needle wash. The LC column used was the BEH amide column (150 × 2.1 mm, 1.7 μm, Waters). The following linear gradient was used: 20% A in acetonitrile for 1.5 min followed by an increase to 60% A over 2.5 min with a further 1 min at 60% A after which the column was re-equilibrated for 1.9 min. After each chromatographic run the column was washed with 30 column volumes of water:acetonitrile (6:4) followed by a further 10 column volumes of acetonitrile:water (95:5) for storage. The total run time was 7 min, the flow rate was 0.6 mL/min and the injection volume was 5 μL. In order to resolve pentose phosphates for the identification of ribose-1-phosphate a shallower gradient was employed: 30% A in acetonitrile for 2.0 minutes followed by an increase to 50% A over 3.0 minutes with re-equilibration for 1.9 minutes.

GC-MS and LC-MS data processing

GC–MS and LC-MS chromatograms were analysed using Xcalibur, version 2.0 (Thermo Fisher), integrating each peak individually. GC-MS Peaks were normalised to total area, while LC-MS peaks were normalised to the internal standard.

Multivariate analysis of metabolite profiles

The set of metabolic profiles obtained were analysed by multivariate analysis. Datasets were imported into SIMCA-P 15.0 (Sartorius AG, Gottingen, Germany) for processing using PCA and PLS-DA (a regression extension of PCA used for supervised classification). GC-MS data were scaled to unit variance by dividing each variable by $1/(S_k)$.

Univariate statistical analysis

Univariate statistical analyses were performed using Excel (Microsoft). Values are expressed as mean ± S.D. and the significance level was set at $p<0.05$. For comparisons of three groups, one-way ANOVA was used with a Tukey test with Bonferroni correction as a post-test.* $0.05> p < 0.01$; ** $0.01> p < 0.001$.

Supplemental References

Cader, M.Z., de Almeida Rodrigues, R.P., West, J.A., Sewell, G.W., Md-Ibrahim, M.N., Reikine, S., Sirago, G., Unger, L.W., Iglesias-Romero, A.B., Ramshorn, K., et al. (2020). FAMIN Is a Multifunctional Purine Enzyme Enabling the Purine Nucleotide Cycle. Cell *180*, 278-295 e223.

Carroll, T.D., Langlands, A.J., Osborne, J.M., Newton, I.P., Appleton, P.L., and Nathke, I. (2017). Interkinetic nuclear migration and basal tethering facilitates post-mitotic daughter separation in intestinal organoids. J Cell Sci *130*, 3862-3877.

Cox, J., and Mann, M. (2008). MaxQuant enables high peptide identification rates, individualized p.p.b.-range mass accuracies and proteome-wide protein quantification. Nat Biotechnol *26*, 1367-1372.

Cox, J., Neuhauser, N., Michalski, A., Scheltema, R.A., Olsen, J.V., and Mann, M. (2011). Andromeda: a peptide search engine integrated into the MaxQuant environment. J Proteome Res *10*, 1794-1805.

Frezza, C., Cipolat, S., and Scorrano, L. (2007). Organelle isolation: functional mitochondria from mouse liver, muscle and cultured fibroblasts. Nat Protoc *2*, 287-295.

Honda, T., Yoshizawa, H., Sundararajan, C., David, E., Lajoie, M.J., Favaloro, F.G., Jr., Janosik, T., Su, X., Honda, Y., Roebuck, B.D., et al. (2011). Tricyclic compounds containing nonenolizable cyano enones. A novel class of highly potent anti-inflammatory and cytoprotective agents. J Med Chem *54*, 1762-1778.

Knatko, E.V., Ibbotson, S.H., Zhang, Y., Higgins, M., Fahey, J.W., Talalay, P., Dawe, R.S., Ferguson, J., Huang, J.T., Clarke, R., et al. (2015). Nrf2 Activation Protects

against Solar-Simulated Ultraviolet Radiation in Mice and Humans. Cancer Prev Res (Phila) *8*, 475-486.

Perez-Riverol, Y., Csordas, A., Bai, J.W., Bernal-Llinares, M., Hewapathirana, S., Kundu, D.J., Inuganti, A., Griss, J., Mayer, G., Eisenacher, M., et al. (2019). The PRIDE database and related tools and resources in 2019: improving support for quantification data. Nucleic Acids Res *47*, D442-D450.

Sato, T., Vries, R.G., Snippert, H.J., van de Wetering, M., Barker, N., Stange, D.E., van Es, J.H., Abo, A., Kujala, P., Peters, P.J., et al. (2009). Single Lgr5 stem cells build crypt-villus structures in vitro without a mesenchymal niche. Nature *459*, 262-265.

Shevchenko, A., Tomas, H., Havlis, J., Olsen, J.V., and Mann, M. (2006). In-gel digestion for mass spectrometric characterization of proteins and proteomes. Nat Protoc *1*, 2856-2860.

Szklarczyk, D., Gable, A.L., Lyon, D., Junge, A., Wyder, S., Huerta-Cepas, J., Simonovic, M., Doncheva, N.T., Morris, J.H., Bork, P., et al. (2019). STRING v11: protein-protein association networks with increased coverage, supporting functional discovery in genome-wide experimental datasets. Nucleic Acids Res *47*, D607-D613.

Taguchi, K., Maher, J.M., Suzuki, T., Kawatani, Y., Motohashi, H., and Yamamoto, M. (2010). Genetic analysis of cytoprotective functions supported by graded expression of Keap1. Mol Cell Biol *30*, 3016-3026.

Torrente, L., Sanchez, C., Moreno, R., Chowdhry, S., Cabello, P., Isono, K., Koseki, H., Honda, T., Hayes, J.D., Dinkova-Kostova, A.T., et al. (2017). Crosstalk between NRF2 and HIPK2 shapes cytoprotective responses. Oncogene *36*, 6204-6212.

Tyanova, S., Temu, T., Sinitcyn, P., Carlson, A., Hein, M.Y., Geiger, T., Mann, M., and Cox, J. (2016). The Perseus computational platform for comprehensive analysis of (prote)omics data. Nature methods *13*, 731-740.

Wang, X., West, J.A., Murray, A.J., and Griffin, J.L. (2015). Comprehensive metabolic profiling of age-related mitochondrial dysfunction in the high-fat-fed ob/ob mouse heart. J Proteome Res *14*, 2849-2862.

West, J.A., Beqqali, A., Ament, Z., Elliott, P., Pinto, Y.M., Arbustini, E., and Griffin, J.L. (2016). A targeted metabolomics assay for cardiac metabolism and demonstration using a mouse model of dilated cardiomyopathy. Metabolomics *12*, 59.